



Eclipse Timing Variations of Circumbinary Substellar Objects in TESS Data

EKREM M. ESMER ^{1,2} AND TANSU DAYLAN ¹

¹*Department of Physics and McDonnell Center for the Space Sciences, Washington University, St. Louis, MO 63130, USA*

²*Department of Astronomy and Space Sciences, Faculty of Science, Ankara University, 06100 Ankara, Türkiye*

ABSTRACT

Circumbinary planets and brown dwarfs form in complex gravitational environments, offering insights into formation, orbital stability, and habitability prospects. However, they remain underrepresented, with only 60 confirmed or candidate systems known. In this work, we leverage TESS photometry to search for circumbinary companions through eclipse timing variations (ETVs), analyzing 152 detached eclipsing binaries. By modeling eclipse timings, we identify 26 systems with significant periodic signals, 14 of which have false alarm probabilities below 0.01. While no detections are confirmed, TIC 350297040 emerges as a candidate for a circumbinary brown dwarf ($0.06 M_{\odot}$) under the assumption of a $1 M_{\odot}$ binary system, though further investigation is required. Simulations using synthetic ETVs indicate a 5% recovery rate for circumbinary brown dwarfs and 0.1% for Jupiter-like planets, with median masses of $56.6^{+16.5}_{-23.4} M_J$ and periods of 1404^{+1361}_{-953} d. Our simulations show that the smallest detectable mass is $1.6 M_J$ at a period of 1860 d and confirm that ETV methods are effective in detecting misaligned systems. In the absence of a detection, we set an upper limit of 40% on the occurrence rate of circumbinary brown dwarfs at the 2σ confidence level, while a confirmed single detection would imply an occurrence rate of 13.08%. These constraints are consistent with previous abundance estimates for circumbinary brown dwarfs ($\lesssim 6.5\%$) but motivate a larger sample size. Furthermore, the very low recovery rates provide insights into the debate on first- and second-generation planet formation around post-common envelope binaries.

Keywords: Eclipsing binary stars (444), Timing variation methods (1703), Exoplanet detection methods (489), Exoplanets (498), Brown dwarfs (185)

1. INTRODUCTION

Circumbinary planets are fascinating due to their unique formation mechanisms (Marzari & Thebault 2019; Coleman et al. 2024), dynamical evolution (Correia et al. 2016; Hamers et al. 2016), and potential for habitability (Haghighipour & Kaltenegger 2013). Despite the growing number of confirmed exoplanets, now exceeding ~ 5800 , circumbinary planets and brown dwarfs remain rare, with only 60 confirmed or candidate systems (Baştürk et al. 2023; Esmer et al. 2024, NASA Exoplanet Archive¹). This disparity raises questions about their abundances and detectability (Armstrong et al. 2014; Fleming et al. 2018). Despite their small numbers, the current circumbinary population spans

a wide range of masses, from brown dwarfs (Benedict & Harrison 2017) to Earth-sized planets (Orosz et al. 2019).

Circumbinary systems are also of significant theoretical interest, as they challenge traditional models of planetary formation and stability. This is particularly evident in post-common-envelope binary (PCEB) systems, where planets may form as first- or second-generation objects (Zorotovic & Schreiber 2013; Bear & Soker 2014). Dynamical studies reveal their complex orbital behaviors, including constraints on stability, dynamical evolution, and inclination effects, which influence both the survival of planets and their detectability (Foucart & Lai 2013; Chavez et al. 2015; Correia et al. 2016; Hamers et al. 2016; Quarles et al. 2018; Chen et al. 2023, 2024; Wang & Liu 2024). Additionally, circumbinary systems may contribute to the population of free-floating planets due to planet-ejecting orbital instabilities (Coleman 2024).

ekrem@wustl.edu

¹ <https://exoplanetarchive.ipac.caltech.edu/>

Although the current population of circumbinary planets is largely underrepresented by terrestrial planets, these systems remain compelling for habitability studies. Their unique orbital dynamics often result in complex insolation patterns, which influence their potential to host life (Haghighipour & Kaltenegger 2013; Kane & Hinkel 2013; Simonetti et al. 2020; Graham et al. 2021).

While other detection techniques, such as radial velocity (Standing et al. 2023) and microlensing (Bennett et al. 2016), are increasingly effective in identifying circumbinary planets, the discovery of these systems has primarily relied on two methods: transit photometry and eclipse timing variations (ETVs). Together, these techniques have contributed to the detection of 31 circumbinary planets, 17 of which were identified using ETVs. ETVs are particularly advantageous for detecting massive companions around eclipsing binaries, as they measure variations in stellar eclipse timings caused by the gravitational influence of unseen objects. Their effectiveness in detecting circumbinary brown dwarfs and planets has been tested by some studies (Getley et al. 2021; Sybilski et al. 2010). Precise determination of mid-eclipse times is critical for ETV analyses, requiring high-accuracy measurements (Mikulášek et al. 2014; Deeg & Tingley 2017; Deeg 2020; Esmer et al. 2022).

Efforts to detect circumbinary objects employ various methods, including transit searches (Windemuth et al. 2019), direct imaging (Bonavita et al. 2016), and radial velocity (Martin et al. 2019). Additionally, significant efforts focus on searches utilizing ETVs, which remain a prominent tool in circumbinary researches (Pribulla et al. 2012; Borkovits et al. 2015; Bours et al. 2016; Borkovits et al. 2016; Papageorgiou et al. 2021; Baştürk et al. 2023; Esmer et al. 2024; Mitnyan et al. 2024; Moharana et al. 2024).

The advent of space-based observatories such as TESS (Ricker et al. 2015) has significantly advanced the search for circumbinary planets. With its high photometric precision and extensive sky coverage, TESS has become an indispensable tool for detecting circumbinary systems through both transits (Guerrero et al. 2021) and ETVs (Marcadon & Prša 2024).

Previous studies on the abundance of circumbinary planets have primarily relied on transit (Armstrong et al. 2014; Martin & Triaud 2014) and radial velocity methods (Martin et al. 2019), which are more sensitive to shorter-period planets. In contrast, the ETV method is better suited for detecting massive companions on wider orbits, mainly through the light-travel time effect (LiTE). Figure 1 illustrates how circumbinary gas giants detected via different methods occupy distinct re-

gions in mass-period space, demonstrating the unique role of ETVs in probing long-period systems. Given this sensitivity, determining occurrence rates using the ETV method provides crucial constraints on the population of massive circumbinary companions that may otherwise remain undetected.

With these perspectives, we conduct an ETV-based search for circumbinary substellar objects to characterize their properties and assess their detectability. We model ETVs for a target sample to detect potential circumbinary hosts and provide insights into ETV properties. By running simulations, we determine the efficiency of the ETV method for different system architectures and provide constraints on the population of circumbinary brown dwarfs and planets. This study is an initial step toward a comprehensive analysis of ETV detectability and the statistical occurrence of substellar-mass circumbinary objects.

2. METHODOLOGY

We aim to model and analyze ETVs in binary systems, first by characterizing ETVs within our target sample and then by simulating eclipsing binaries with circumbinary companions to assess detection rates.

We begin by selecting binary systems based on eclipse features for precise timing analysis, followed by processing light curves to ensure high data quality. Next, we model the primary eclipses in each target to estimate mid-eclipse times and then analyze the ETVs to detect periodicities within the data. Finally, we simulate synthetic binary systems with circumbinary objects to evaluate the detectability of these companions based on the ETV signals generated.

2.1. Target Selection

We identified our target sample from the TESS Eclipsing Binary Catalog² (TEBC, Prša et al. 2022), focusing on detached binaries due to their eclipse shape allowing for more precise timing determinations compared to semi-detached and contact binaries. We used the morphology parameter from the TEBC to filter the systems, selecting only those with `morphology` < 0.2. We limited the binary periods to less than 14 days to capture at least one eclipse within a given TESS sector. The minimum binary period in the sample was 1.5 days.

We filtered out targets with relative period uncertainties of 10^{-4} or larger to obtain precise period determinations. We also included targets with established reference eclipse times and associated uncertainties. The

² <https://tessebs.villanova.edu/>

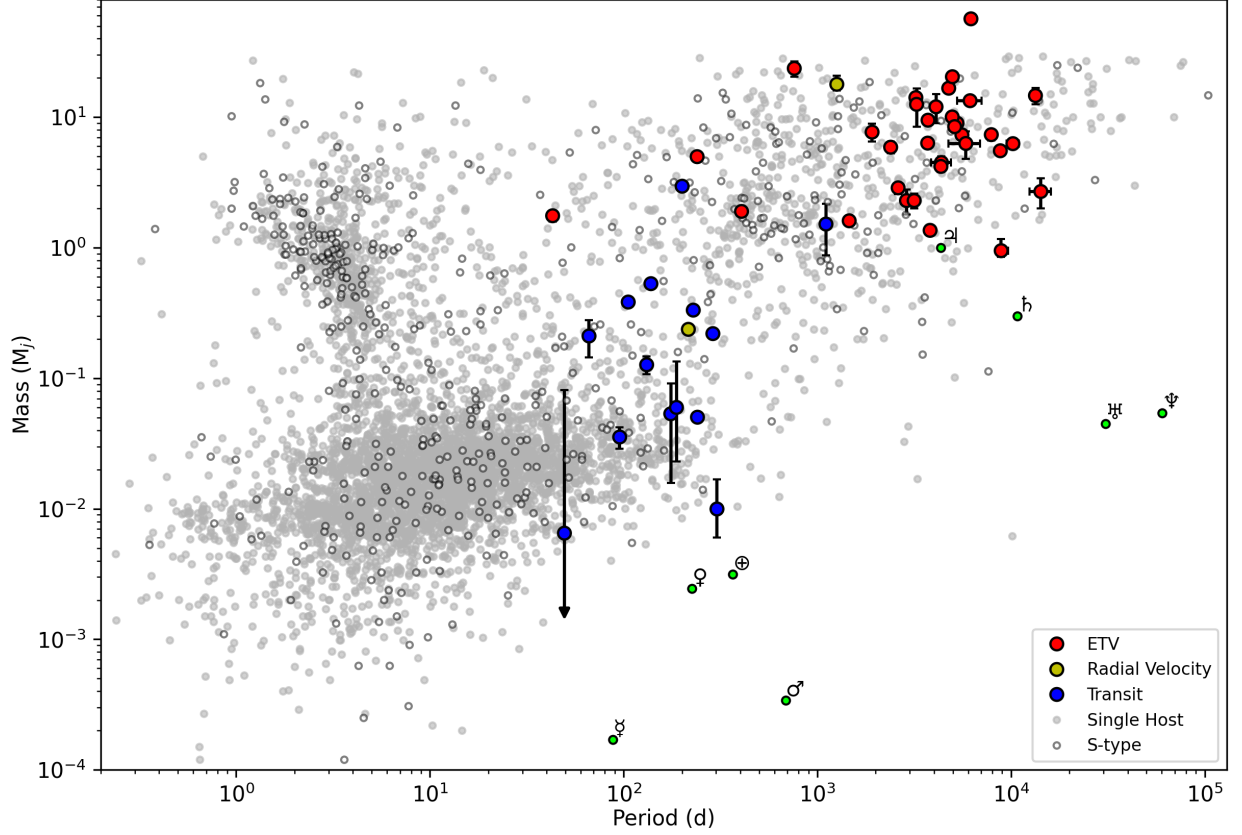


Figure 1. Mass (either projected or true) vs orbital periods of circumbinary (p-type) brown dwarf and planet population derived from NASA Exoplanet Archive, Baştürk et al. (2023) and Esmer et al. (2024) including candidates along with i) all known single host planets, ii) planets with s-type orbits in multiple star systems and iii) planets of the Solar system (green markers).

target sample consisted of 310 systems with TESS magnitudes ranging from 5 to 16.

2.2. Data Preparation

To analyze the eclipse timing of our target binaries, we retrieved and processed their light curves from TESS observations accessed via the Mikulski Archive for Space Telescopes (MAST)³ portal. For this study, we used Simple Aperture Photometry (SAP) fluxes, as the Pre-search Data Conditioning SAP (PDCSAP) fluxes can introduce artificial trends that may distort the intrinsic features of eclipsing binary light curves. We collected only 2-minute exposures for each target, with the last observation for any target occurring in TESS Sector 80.

The data preparation involved removing NaN values to exclude incomplete measurements, selecting data points with a quality flag of zero to retain only high-quality observations, and normalizing each light curve to its median value.

2.3. Eclipse Light Curves

To determine the eclipse parameters of the target binaries, we modeled their light curves using the *allesfitter* (Günther & Daylan 2021, 2019) code with a Markov Chain Monte Carlo (MCMC) approach. Initial values for the orbital period and time of the primary eclipse were taken from the TEBC. The free parameters included the radius ratio, the sum of stellar radii over the semi-major axis, the cosine of the inclination, the time of the primary eclipse, the orbital period, the quadratic limb darkening coefficients, and the logarithm of the flux error. We fitted only the primary eclipses and iteratively selected the light curves within a phase range centered on zero. We extended $\pm 1/4$ of the orbital period, ensuring that the primary eclipse was included in the selected data. To model the flux baseline for the eclipses, we applied splines to the out-of-eclipse regions surrounding each primary eclipse.

To minimize the accumulation of uncertainties on the linear ephemeris, we modeled only the eclipses in each target's first and last available TESS sectors, limiting

³ <https://mast.stsci.edu/>

the analysis to 6 primary eclipses to reduce computation time.

When sampling from the posterior of the model parameters using MCMC, we used 300 walkers, discarded 27,000 samples as burn-in, and retained 5,000 steps. This process generated distributions for each free parameter, allowing us to quantify median values and uncertainties. We used these eclipse models in the next step to determine eclipse mid-times.

2.4. Eclipse Timing Calculations

To calculate the mid-times of the eclipses, we used the primary eclipse model of each target, relying on parameters obtained from our previous light curve modeling and using Markov Chain Monte Carlo (MCMC) implemented via `allesfitter`. Initial values for parameters were taken from the previous modeling phase: the radius ratio, the sum of stellar radii over the semi-major axis, the cosine of the inclination, the time of the primary eclipse, the orbital period, the quadratic limb darkening coefficients, and the logarithm of the flux error. For the mid-time calculation, we fixed the time of the primary eclipse and orbital period, keeping the remaining parameters free to capture light curve variations across cycles. A spline was used to model the out-of-eclipse regions to maintain a stable baseline, consistent with the previous flux baseline modeling step.

When estimating the posterior mid-time via MCMC, we used a number of walkers set to four times the number of eclipses, with a minimum of 40 walkers. We discarded 15,000 steps as burn-in and retained the subsequent 5,000 steps to sample from the posterior. This fitting process yielded mid-times for each primary eclipse, allowing us to quantify deviations with associated uncertainties.

2.5. Lomb-Scargle Periodograms of ETVs

To investigate periodic signals in the eclipse timing variations (ETVs) of our target binaries, we conducted a Lomb-Scargle frequency analysis (Lomb 1976; Scargle 1982), allowing us to identify and characterize potential periodic trends. For this purpose, we utilized relevant packages in `astropy` (Astropy Collaboration et al. 2013, 2018, 2022).

We began by filtering the ETV data to exclude mid-time measurements with uncertainties on the order of hours, as these were indicative of unreliable mid-time determinations. We then ran an initial Lomb-Scargle analysis and applied a 3-sigma clipping to the residuals from the strongest periodicities to remove additional outliers, retaining only high-quality data points. Lomb-Scargle analysis was performed for each target only if

more than four mid-time measurements remained after these filtering steps.

Following this process, we successfully analyzed mid-eclipse times for 152 targets, a reduction from the initial sample of 310. This decrease was primarily due to an insufficient number of eclipses in the TESS data, while in some cases, complex light curve features also contributed to exclusion.

To prepare the data for analysis, we fitted a linear model to the time series, using the residuals from this fit to update the linear ephemerides. We then used the Lomb-Scargle periodogram on these residuals, scanning frequencies up to a maximum limit set at four times the binary period. Since our data are separated by multiples of the binary period (P_{bin}), the Nyquist frequency of our dataset is $\frac{1}{2P_{bin}}$ (for further explanation, see VanderPlas 2018). From the periodograms, we identified the frequencies with the highest power. We calculated the corresponding periods, amplitudes, and false alarm probabilities (FAP) of the detected signals, quantifying the statistical significance of the observed periodicity.

2.6. Simulating ETV Systems

In this section, we describe our approach to simulating binary systems with circumbinary companions, aiming to assess the detectability of planets and brown dwarfs using ETVs. We generated realistic parameters for binary systems observable by TESS, assigned properties to circumbinary objects with various orbital and mass distributions, and calculated the resulting ETVs. The simulated binary and circumbinary parameter distributions can be seen in Figure 3, and further explanations can be found in the following two sections. We focused exclusively on timing variations caused by the presence of an additional body, without including secular trends, apsidal motion, or other timing variations related to stellar activity. Using Lomb-Scargle periodogram analyses, we evaluate the effectiveness of ETV methods in detecting these simulated circumbinary objects.

2.6.1. Generating Binary Parameters

We generate the following parameters for binary systems: equatorial coordinates (RA & Dec), brightness, masses of the primary and the secondary, orbital period, reference eclipse time, orbital inclination, and ETV uncertainty.

To simulate realistic ETV data that reflects the TESS sky coverage as a function of celestial coordinates, we gathered coordinate and brightness values for 10^7 stellar objects with $r_p < 14$ from the Gaia Archive (Gaia Collaboration et al. 2016, 2023). We filtered out galaxy and quasar candidates and selected only sources classified as stars, setting the discrete source classifier probability for

stellar sources at `classprob_dsc_combmod_star` > 0.9. To ensure the sample consists of stellar sources, we limited our selection to objects with a parallax signal-to-noise ratio (SNR) greater than 5. To generate a binary, we randomly selected RA and Dec, along with r_p brightness as a proxy to TESS magnitude. We checked if any of these random coordinates were observable with TESS and determined their observation frequency based on the number of sectors they were covered in, using the TESS-Point tool (Burke et al. 2020) (Figure 2). We did not account for contamination from nearby sources due to the TESS pixel size. This effect is especially pronounced near the galactic plane, where most of our sample is located.

We sampled the masses of the companions in a binary system from the initial mass function (IMF) derived for stellar systems by Chabrier (2003). After we sampled a primary star mass, we used that value for an upper limit for the secondary mass and sampled it from the same IMF to ensure that the mass ratio M_2/M_1 stays between (0,1]. The individual masses were selected between 0.1 and 5 solar masses. Therefore, in some cases, the total binary mass exceeds $5M_\odot$. We calculated the radii of the binary components from the mass-radius relationship (Eq. 1) from Gorda & Svechnikov (1998).

$$\log_{10}(R) = \begin{cases} 0.049 + 0.993 \log_{10}(M) & \text{if } M \leq 1.4 \\ 0.096 + 0.652 \log_{10}(M) & \text{if } M > 1.4 \end{cases} \quad (1)$$

We generate binary period from the log-normal period distribution in TEBC, and for the reference eclipse times, we used uniform sampling between \pm binary period. We calculated the eclipse times for each binary and determined the eclipses that were observable in any Sectors based on the beginnings and ends of TESS observations⁴.

We uniformly sampled $\cos i$ between 0 and 1 to obtain randomly oriented orbits. For each simulated binary system, we checked the eclipse condition (Eq. 2) and continued to ETV calculation if satisfied.

$$\cos(i) \leq \frac{R_{pri} + R_{sec}}{\sqrt[3]{(M_{pri} + M_{sec}) \times P_{bin}^2}} \quad (2)$$

To assign timing uncertainties to each generated binary system, we first modeled the logarithm of ETV uncertainties that we derived in Sections 2.4 vs brightnesses with a 2D Gaussian distribution. Based on this model, we sampled uncertainties that correspond to the brightness values for any system.

⁴ <https://tess.mit.edu/observations/>

2.6.2. Generating Circumbinary Objects

We generated the following parameters for the circumbinary objects: mass, orbital period, mean anomaly, and inclination. We assumed circular orbits, hence keeping eccentricity, the argument of periastron, and the longitude of ascending nodes fixed to zero. We separated this stage into two main groups: i) coplanar orbits between the binary (C) and ii) uniform circumbinary orbital inclinations (U). Each of these parts was further divided into two groups based on their masses: planets (PL; 1-13 M_J) and brown dwarfs (BD; 13-80 M_J).

We used the exoplanet mass function from Mordasini (2018) to generate masses less than 13 M_J . This function is a power law and is $\propto M^{-1}$ for masses between 1 – 5 M_J , and $\propto M^{-2}$ for masses larger than 5 M_J . To generate the brown dwarf masses (13 – 80 M_J), we used IMF from Chabrier (2003).

Due to their low ETV amplitudes, we did not extensively simulate masses smaller than 1 M_J . However, we calculated the SNR for the masses of Saturn, Neptune, and Earth on coplanar orbits around random binaries as $10^{-2.4}$, $10^{-3.1}$ and $10^{-4.3} \pm 10^{0.5}$, in respective order. The maximum SNR for Saturn analogs was 0.16 within 2000 random samples.

We sampled the orbital periods of the circumbinary objects from a log-uniform distribution between 10 times the binary period and 6000 days. The inner range should reflect the minimum stable period ratio of a circumbinary, and for our sample, we set the inner limit based on the largest value calculated by Quarles et al. (2018). The larger limit was selected to be approximately three times the data time span. The smaller limit was chosen to ensure the dynamical constraints (though not included in any calculations) would be considered. In the case of large mass and short periods for the circumbinary object, as well as small binary mass, the gravitational interactions between the objects would introduce additional timing variations. We did not simulate this interaction in this study, and the recovery and occurrence regarding these configurations should differ from our results.

For the coplanar orbits, we adopted the binary inclination as the inclination of the circumbinary object. In contrast, we sampled $\cos i$ uniformly between 0 – 1 for the groups of uniform circumbinary orientation. We sampled the mean anomaly from a uniform distribution between $\pm 360^\circ$.

2.6.3. ETVs of Simulated Systems

By using the generated binary and circumbinary parameters, we performed orbital simulations with `rebound` (Rein & Liu 2012) and the IAS15 integrator

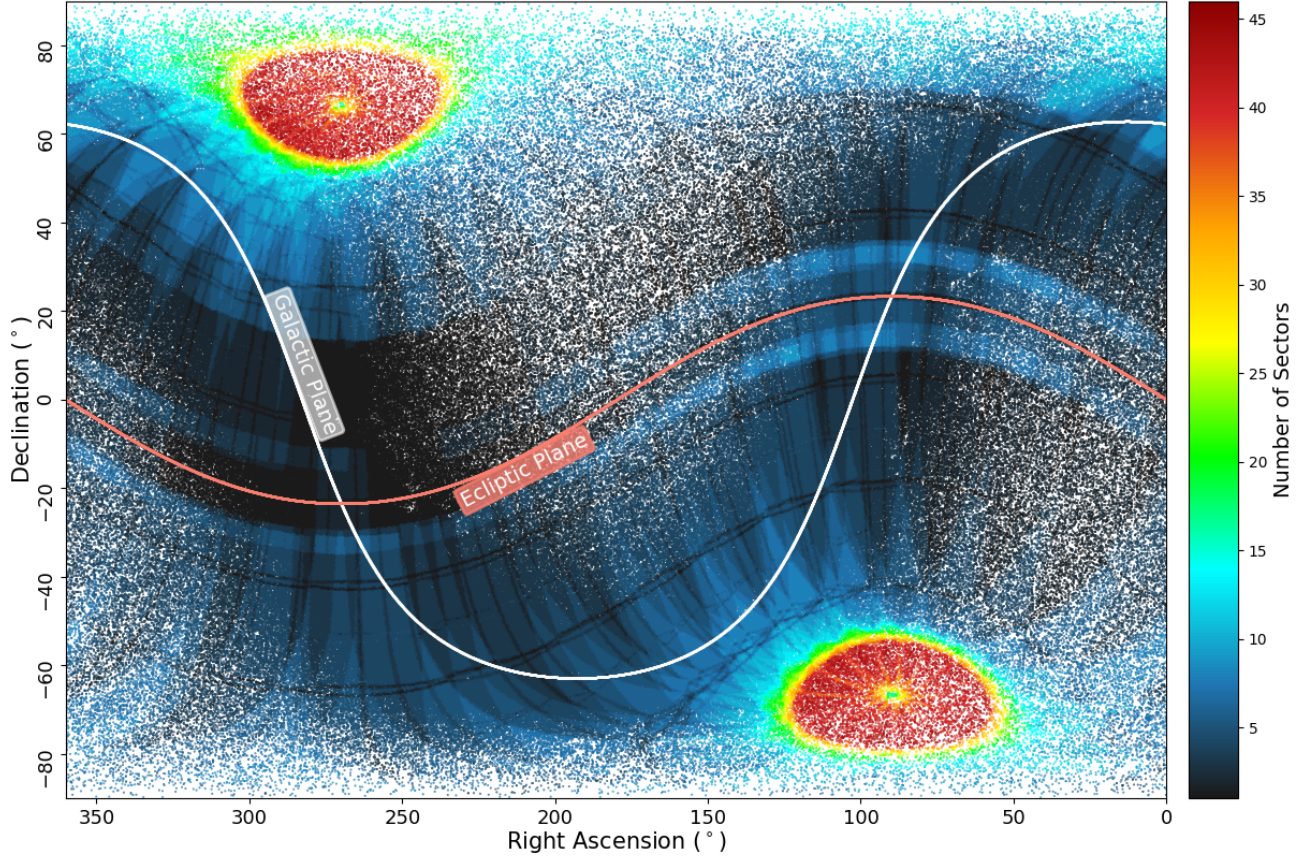


Figure 2. The distribution of the simulated binary sample in the equatorial coordinates with color coding based on the number of TESS sectors. Warmer colors represent areas with higher observational coverage. The TESS Continuous Viewing Zones (CVZs) appear as the red regions near the ecliptic poles.

(Rein & Spiegel 2015). Each binary system was treated as a single object with its total mass, reducing the system to a two-body problem. Eclipse timing variations (ETVs) were calculated from numerical simulations following the method described in Esmer et al. (2023).

For each of the four groups categorized by mass and inclination, we generated 10^6 samples. Among these, 287,472 (7.2%) satisfied the eclipse condition, while the remaining systems were excluded before ETV calculations. Additionally, systems with fewer than four observable eclipses in TESS data were excluded from further analysis.

To simulate ETVs, we added the LiTE model corresponding to each circumbinary system to the eclipse times. We introduced Gaussian scatter to the data based on the timing uncertainties generated for the systems where eclipses are observable with TESS. Similar to analyzing observed data, we fitted a line to ETVs to update linear ephemeris and used the residuals ETVs in the further steps. While we did not add a linear ephemeris difference of any kind - not to binary period nor to reference eclipse times, we implemented the prescribed linear fit to investigate the deviation of the detected periods

and amplitudes from the original values, especially for the cases of undersampled ETVs. We performed Lomb-Scargle analyses of the ETVs and recorded the periods, amplitudes, and FAPs corresponding to the peak frequency in the periodograms. We limited the periodogram between the frequency corresponding to four times the binary period and two times the available data range for each system. All of the steps explained in this paragraph were repeated three times, and only the results with the highest FAP values were saved to decrease the number of false positives.

3. RESULTS

3.1. Results of ETV Analyses of the Target Sample

We use FAP values in the ETV periodograms of our targets as indicators of signal significance. While defining a strict FAP threshold to distinguish true positives from false positives is challenging and not necessarily robust, we employ FAP as a quantitative measure of the reliability of our ETV search. This approach is necessary since we lack additional statistics from an extensive ETV analysis -such as detailed model fitting, model comparisons, and other statistical methods- that

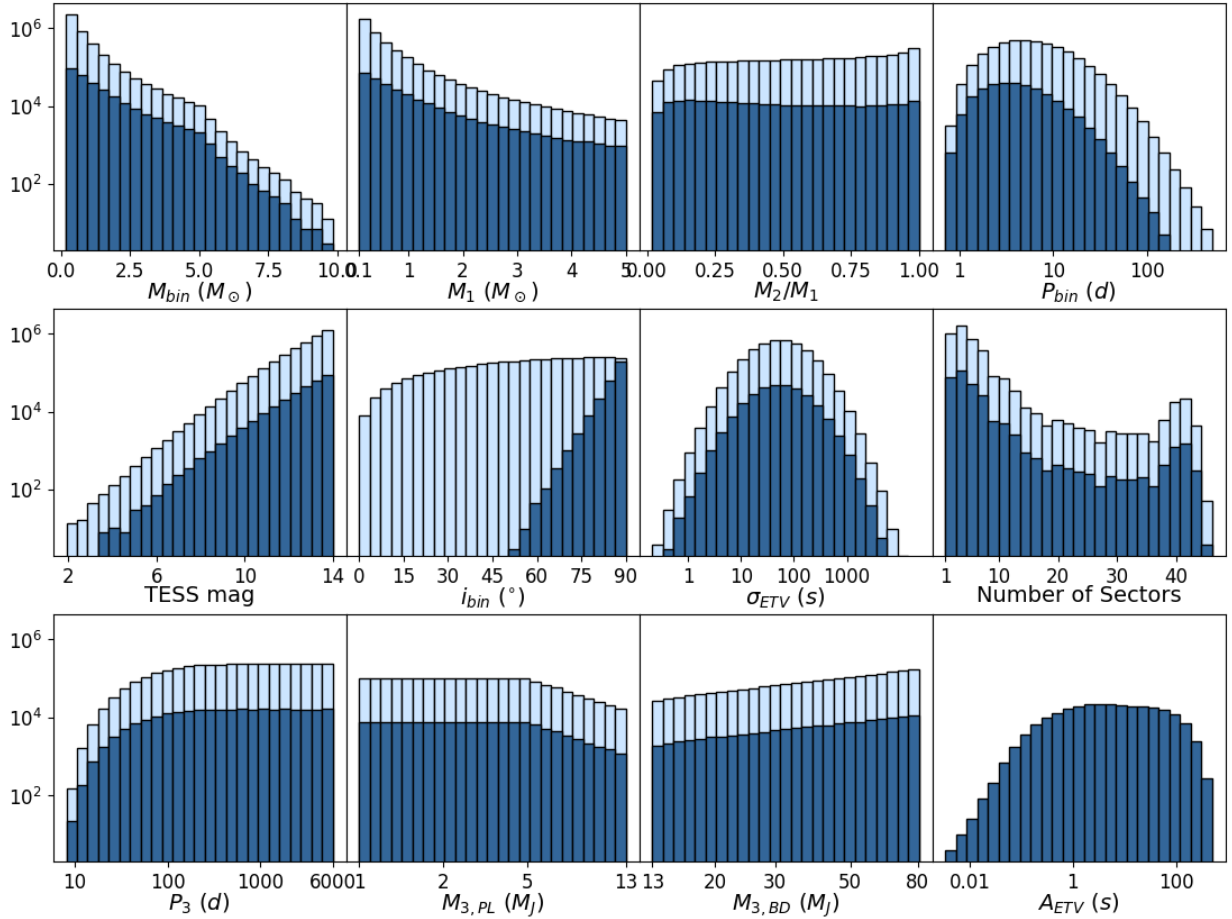


Figure 3. Distributions of the simulated binary and circumbinary parameters. The subscripts *bin*, *1*, *2*, *3*, *PL*, and *BD* correspond to parameters related to the binary system, primary star, secondary star, circumbinary object, planet mass, and brown dwarf mass, respectively. Note that all vertical axes are logarithmic, while some horizontal axes are also logarithmic. The full set of 4×10^6 samples is represented in light color, while the eclipsing binary sample (287,472 systems, or 7.2%) is shown in dark color. The ETV amplitude (A_{ETV}) values were calculated only after a binary eclipse condition was satisfied; therefore, this parameter is displayed exclusively in dark colors. Other binary and circumbinary parameters were sampled from uniform distributions and are not shown here. See Sections 2.6.1 and 2.6.2 for further details.

are typically feasible for studies of individual targets, as demonstrated in Esmer et al. (2021, 2022). FAP represents the probability that detected frequencies arise from noise, with values close to 1 indicating such cases. Most of our targets display peak frequencies with FAP values near 1. Only 26 targets exhibit FAP values below 0.1, and 14 fall below 0.01. This section discusses notable targets based on their ETV periodograms or light curve solutions. The periods, amplitudes, and FAP values of our targets can be seen in Table 2, while the ETV diagrams, along with the Lomb-Scargle models, can be seen in the Appendix.

To estimate the types of third bodies that could generate such ETVs, we calculated hypothetical third-body masses by assuming total binary masses of $1 M_\odot$ and $2 M_\odot$ for each target with a FAP below 0.1. We considered only the LiTE effect and based these calculations on the periods and amplitudes correspond-

ing to the periodicities in the ETVs. Calculations were performed using Equation 4 from Borkovits et al. (2015), assuming circular orbits and an inclination of 90° for the hypothetical third bodies - i.e., minimum or projected mass. The resulting third-body masses fall below the stellar mass limit of $\sim 0.08 M_\odot$ for TIC 270648838 ($0.05 M_\odot$), TIC 142979644 ($0.05 M_\odot$), and TIC 166090445 ($0.07 M_\odot$) for a binary mass of $2 M_\odot$; and for TIC 3816260 ($0.06 M_\odot$), TIC 350297040 ($0.06 M_\odot$), and TIC 140659980 ($0.07 M_\odot$) for a binary mass of $1 M_\odot$. However, the ETV variations of these systems, except for TIC 350297040, are most likely caused by stellar variation, apsidal motion, or sampling effects, as we will discuss further in this section.

One of the targets in our study, TIC 170344769 (also known as Kepler-1647), is an eclipsing binary system with an 11.3-day orbital period and a known circumbinary planet orbiting approximately every 1100 days. In

our Lomb-Scargle analysis, we were unable to detect a strong periodic signal near the planet’s orbital period. Instead, the frequency with the maximum power corresponds to a period of 49 days, with a FAP of 0.6, indicating that the detected signal is likely insignificant. Similarly, this planet was also not detected through eclipse timing variations in the discovery study by [Kostov et al. \(2016\)](#).

For TIC 364120439, we obtained a relatively small radius ratio of around 0.12. However, the primary star is evolved, with an effective temperature of approximately 4800 K and a surface gravity ($\log g$) of about 3.1, indicating a stellar companion. In TIC 323301918, the periodogram shows the strongest peak at 236 days with a FAP of 0.02. TIC 258918831 has a high Gaia renormalised unit weight error (RUWE) value of 37.4; its periodogram indicates the strongest peak at 30 days, albeit with a FAP of 0.43. Lastly, for TIC 103452621, the strongest periodogram peak corresponds to a period of 160 days with a FAP of 0.08. This system’s light curve exhibits oscillations on the order of an hour, likely altering each eclipse individually and contributing to the observed 160-day variation in the timing data.

The FAP value in the periodogram for TIC 26542657 is among the lowest in our targets. The strongest peak corresponds to a period of 1141 days with a FAP of 10^{-11} . The ETV trend is cyclic and resembles a sine wave, with an amplitude of 31.8 minutes. Interestingly, the eclipse light curves are primarily V-shaped in TESS Sectors 14 and 15 but transition to total eclipses in the remaining TESS sectors. The eclipse durations also increase in line with these variations in the light curves. The system’s Gaia RUWE is 4.4, and with all these indicators, the system may be undergoing dynamical interaction requiring further investigation.

TIC 230063769 exhibits periodicity in its ETV, with a low FAP of 0.002. The corresponding period is 38 days with an amplitude of 29 seconds. The binary’s orbital period is 8.26 days, making the ETV periodicity approximately 4.6 times the orbital period. However, the light curve of this system shows a prominent out-of-eclipse variation that likely causes the observed ETV variation.

The ETV analysis of TIC 3816260 suggests a periodic signal; however, given the limited number of observed eclipses and potential sampling biases, the detected variation is likely influenced by data sparsity rather than a real third-body companion. While the calculated circumbinary mass based on Lomb-Scargle results corresponds to substellar masses, the lack of sufficient data points makes the Lomb-Scargle analysis less robust, in-

creasing the possibility that the periodicity is an observational artifact.

For TIC 198537349, we observed a very low FAP of 5×10^{-8} in the periodogram, with a corresponding ETV period of 283 days and an amplitude of 47 seconds. The light curve of this system lacks a secondary eclipse, which could be due to either an eccentric orbit with a periastron near the primary eclipse, an intense brightness contrast between the binary components that hide the secondary eclipse within the photometric scatter, or two nearly identical companions producing consecutive primary eclipses.

TIC 373915220 exhibits a prominent ETV variation with a FAP of 5×10^{-27} , although the variation is longer than the available data coverage of approximately 1200 days. The binary’s orbit appears eccentric, with the secondary eclipse occurring at phase 0.54 instead of 0.5. The phased light curves for both the primary and secondary eclipses show a similar trend, which does not support apsidal motion as the cause of the observed ETV variation. The mostly flat light curve for out-of-eclipse intervals suggests either a secular trend or the presence of an additional body as the likely cause of the timing variation.

The periodogram of TIC 140659980 shows its strongest frequency at a period of 407 days with a FAP of 0.03 and an amplitude of 37 seconds. The light curve exhibits substantial out-of-eclipse variation, and the eccentric orbit makes a circumbinary explanation less likely, warranting further investigation.

TIC 300161053 has a promising ETV variation with a FAP of 0.0002. The corresponding period is 1430 days with an amplitude of 44 minutes, although it is strongly undersampled. The timing data has two distant parts, both with a decreasing trend. There is a possibility that the correct ETV period is a harmonic of the detected signal, while the true amplitude may also differ considerably. The binary has an eccentric orbit, which hints that apsidal motion can be a driving mechanism of the observed timing variation.

Another clear ETV trend is present for TIC 237944385, with a FAP of 6×10^{-20} . If this variation is periodic, it likely has a period longer than the current TESS coverage. Only three chunks of data are spread evenly across approximately 1500 days, with a variation amplitude of at least 4 minutes.

The peak frequency in TIC 278988794’s periodogram corresponds to a period of 740 days and an amplitude of 3.4 minutes, with a FAP of 0.0006. The phased timing data still lacks one-half of this periodicity, suggesting that the true period may be a harmonic of the detected

frequency, and the amplitude may be larger than detected.

Another longer-than-data-range variation is present in TIC 102929927, with a FAP for the peak frequency of 2×10^{-11} . The corresponding period and amplitude are 2536 days and 6.3 minutes, respectively. The variation resembles either a trough in a cyclic trend or a secular one. The timing data is well-distributed throughout the trend, indicating that high-order harmonics are unlikely in the periodogram.

TIC 407584737 has an ambiguous periodicity of 30.9 days with an amplitude of 2.6 minutes. The FAP of this variation is 0.02. Given the significant out-of-eclipse variation and the fact that the ETV variation is only 5.5 times the orbital period, we believe that the detected variation likely reflects out-of-eclipse photometric variation.

TIC 180412528 has a peak frequency corresponding to a period of 78 days and an amplitude of 18 seconds, with a FAP of 0.02. This binary has frequent flares in its light curve and strong out-of-eclipse variation, potentially causing the detected timing variation.

TIC 167692429 was identified as a compact hierarchical triple system by Borkovits et al. (2020). The peak period we detected (328 days) closely matches the period calculated by Borkovits et al. (2020) at 331 days. In addition to the TESS observations used by Borkovits et al. (2020) (Sectors 1-4, 6-13), we incorporated data from Sectors 61-68. The ETV data from these sectors captures only the downward phase of the cyclic variation. The light curves for Sectors 61-68 show a decreasing eclipse depth for both the primary and secondary eclipses, further confirming the complex dynamics of this system.

A target with a strong periodogram peak is TIC 260502102, with an ETV period of 2593 days, a value exceeding the data coverage. The corresponding amplitude is at least 8.6 minutes, and the variation appears secular rather than cyclic, as the data spans only a parabolic trend over 1900 days. The FAP for this peak is 2×10^{-112} .

The light curve of TIC 118313102 exhibits strong oscillations of pulsation origin, possibly reflected in the timing data with a 41-day periodic variation and a 1-minute amplitude. The FAP of this timing variation is 0.04. A similar case is TIC 219707463, where out-of-eclipse oscillations may induce a timing variation approximately 5 times the binary period, with an amplitude of 18 seconds and a FAP of 0.05.

TIC 142979644 has a light curve with numerous flare-like events and out-of-eclipse oscillations. The system's ETV data shows a variation with a period of 535 days

and an amplitude of 20 seconds, with a corresponding FAP of 2×10^{-7} . Similarly, TIC 166090445 has an ETV variation with a period of 544 days, an amplitude of 28 seconds, and a FAP of 0.001. Although TIC 270648838 lacks flare-like spikes in its light curve, it exhibits substantial out-of-eclipse variations and an ETV variation with a period of 158 days, an amplitude of 8 seconds, and a FAP of 0.04.

3.2. Results for TOIs and KOIs in Our Targets

Our study examined several TESS Objects of Interest (TOIs) and Kepler Objects of Interest (KOIs) within the target sample. Many of these objects displayed characteristics indicative of stellar binaries rather than exoplanetary systems based on their light curve properties, radius ratios, and other inferred parameters. Below, we summarize the notable findings for each of these objects.

While TIC 300871545 (TOI-184) is currently listed as an exoplanet candidate in the NASA Exoplanet Archive, Gaia data (effective temperature $T_{\text{eff}} \sim 6400$ K, surface gravity $\log g \sim 4.2$) combined with our derived radius ratio ($R_2/R_1 \sim 0.15$) suggest it is more likely a stellar binary. The periodogram has its strongest peak around 47 days and a secondary peak around 240 days, both with high FAP values. Although the latter periodicity is visible, no further speculation is made.

The companion of TIC 236387002 (TOI-2119) was confirmed as a brown dwarf by Cañas et al. (2022), and our light curve results align well with their findings. The periodogram shows no significant variations in the ETV.

For TIC 238197709 (TOI-646), we found a radius ratio of $R_2/R_1 \sim 0.26$, suggesting a stellar-size companion around a primary star with $T_{\text{eff}} \sim 5700$ K and $\log g \sim 3.8$. The ETV has a periodicity of 156 days, although the FAP is relatively high at 0.59.

TIC 1400770435 (TOI-1344) has a high radius ratio ($R_2/R_1 \sim 0.49$) around a solar-like star ($T_{\text{eff}} \sim 5900$ K, $\log g \sim 4.2$), indicating a stellar companion. There is no apparent ETV based on visual inspection or its periodogram.

TIC 350743714 (TOI-165, EBLM J0555-57) was classified by von Boetticher et al. (2017) as a Saturn-sized stellar-mass object orbiting a Sun-like star. Our findings are consistent, suggesting a small secondary with a radius ratio of $R_2/R_1 \sim 0.07$.

Based on our light curve models for TIC 382188882 (TOI-276) and TIC 149990841 (TOI-167), we derived radius ratios of ~ 0.48 and ~ 0.47 , respectively, indicating stellar companions around Sun-like primaries. Both objects lack significant frequencies in their ETV periodograms.

TIC 77951245 (TOI-450) was identified as a low-mass, pre-main-sequence binary by [Tofflemire et al. \(2023\)](#). Due to the limited number of available eclipse times (only six), we were unable to conduct a detailed timing variation analysis.

TIC 233390838 (TOI-1341) has a period of 12.9 days in the TEBC, which is double the actual orbital period, as noted in [Schanche et al. \(2019\)](#). Because we adopted the TEBC period, our ETV analysis for this system used only half the timings available in TESS data and showed no significant periodicities.

For TIC 317507345 (TOI-1615), the primary star has Gaia parameters of $T_{eff} \sim 7200$ K and $\log g \sim 4.1$, and our derived radius ratio of $R_2/R_1 \sim 0.35$ suggests a stellar-sized companion. The ETV diagram shows no significant periodicity.

TIC 101395259 (TOI-623) includes a $1.17M_\odot$ primary and a $0.098M_\odot$ secondary as noted by [von Boetticher et al. \(2019\)](#). Due to the limited number of mid-eclipse times, we were unable to identify any significant periodicities in the periodogram.

Some of our remaining targets are also TOIs, for which we either only modeled their light curves; TIC 280206394 (TOI-677), TIC 321857016 (TOI-1420), and TIC 232967440 (TOI-1173) - or primarily analyzed their timing data, as in the case of TIC 277683130 (TOI-138). However, no significant variations or notable features were identified for these targets.

Some of our targets were identified as KOIs and classified as false positive candidates for transiting exoplanets: TIC 137549183, TIC 274129522, TIC 159720778, TIC 27006880, TIC 27915909, TIC 159047480, and TIC 184298625. Among these, TIC 159720778 and TIC 184298625 exhibited the strongest frequency signals in our Lomb-Scargle analysis, with FAP values of 0.099 and 0.0005 and corresponding periods of 48 days and 413 days, respectively. In contrast, the remaining targets showed their strongest frequency signals with FAP values close to 1, indicating no significant periodic signals.

3.3. Results for ETV Simulations

The successful detection of a simulated circumbinary companion is characterized primarily by a detected period and amplitude that closely match the true parameter values or their harmonics or subharmonics. To evaluate this, the results of our simulations for each sample were analyzed using ratio distributions of detected and true values for periods and amplitudes. Additionally, FAP must be low ($FAP \ll 1$), as it quantifies the likelihood that the detected signal arises from random noise (i.e., a false positive).

The distributions of detected vs true period and amplitude ratios for the CBD group are shown in Figure 4. Most of the recovered periods and their amplitudes with $FAP \ll 1$ pile up around 1:1 ratio regions. However, a considerable amount of them form a tail towards smaller ratios. The tail-forming data are mostly for true periods larger than the total data time span for any individual target (maximum of ~ 1800 days). The tail becomes pronounced especially when the true period reaches ~ 3000 days, and an upper limit for detected vs true values of period and amplitudes arises around 1:1 (turquoise circles in Figure 4). The overall features for the UBD group are similar to the CBD group, while the number of detections diminishes considerably for planetary masses (UPL & CPL) along with distinguishable features. Therefore, we construct the final detection conditions and thresholds based on CBD and UBD groups.

A threshold for the detected-to-binary period ratio is essential to address stability concerns in circumbinary systems. As shown in [Quarles et al. \(2018\)](#), the inner limit for a stable circumbinary orbit depends on parameters such as stellar masses, mass ratio, eccentricity, and other binary properties. We adopted a minimum value of four times the binary period limit in the Lomb-Scargle period search of simulated systems for the shortest period limit. However, we observed a significant clustering of detected signals near this limit, which we interpret as failed circumbinary detections. To eliminate these false positives, we applied a threshold that requires the detected-to-binary period ratio to exceed five, thereby retaining only signals with higher values.

We set an SNR threshold of 1 to filter out spurious results, selecting only data above this limit. Specifically, the signal is defined as the amplitude calculated from the Lomb-Scargle analysis, while the noise is characterized by the ETV scatter used to generate the simulated data noise. Data with $SNR < 1$ consistently corresponded to $FAP \gg 0$, and to further filter out false positives, we set a maximum FAP limit of 0.1, focusing on statistically significant variations.

In addition to applying the detected-to-binary period ratio, SNR, and FAP thresholds, we investigated the detected-to-true amplitude and period ratios, focusing on values around 1. As previously mentioned, most data concentrate near a ratio of 1:1, while there are (i) less populated clusters around harmonics and subharmonics and (ii) a linear correlation between the two ratios. Both behaviors become more pronounced when filtering out the data corresponding to true periods longer than approximately 3000 days. To define a region that avoids being overly conservative and excluding potential successful detections while not being too broad and

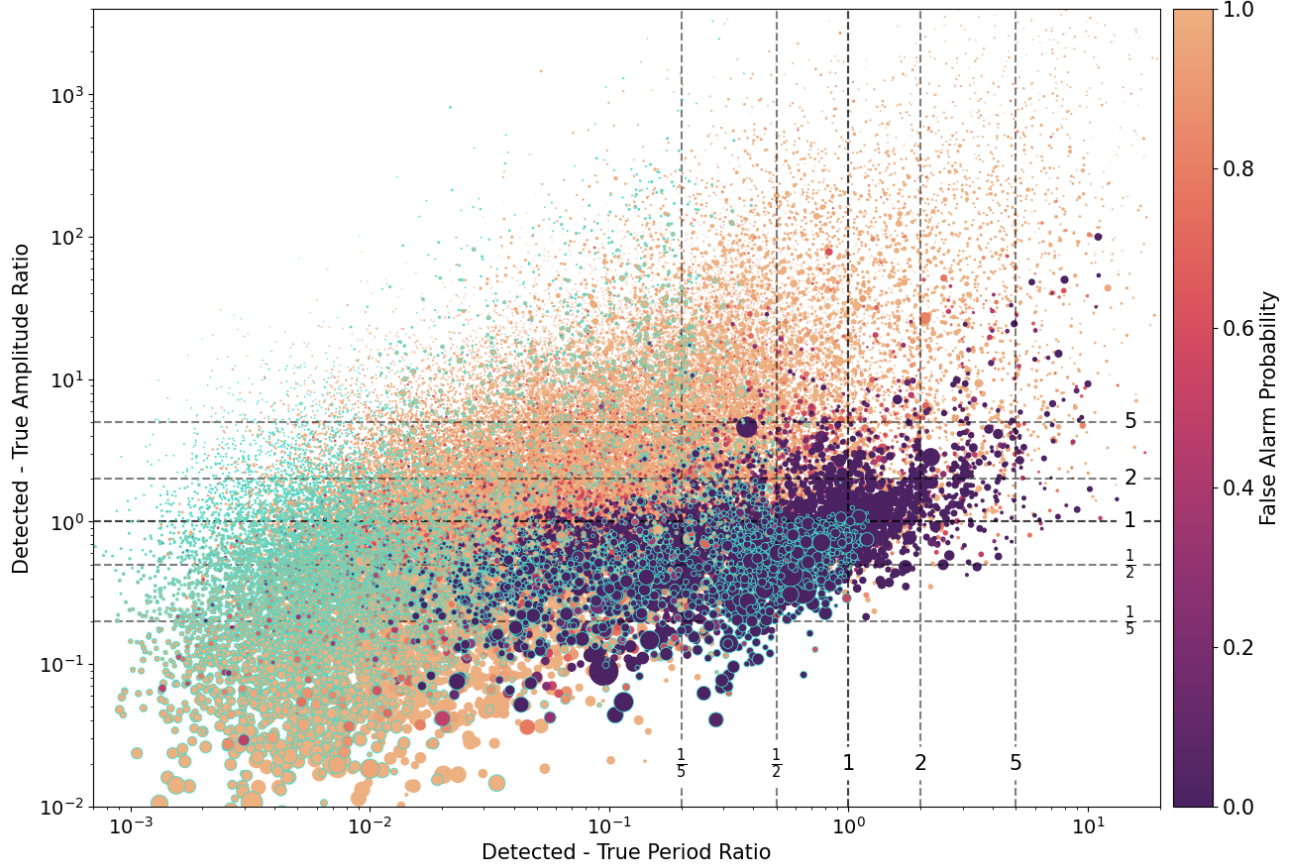


Figure 4. Correlation between detected-to-true period ratio and amplitude ratio across data points for the coplanar & brown dwarf (CBD) group. The color scale represents False Alarm Probability (FAP), with darker points indicating lower FAP values. Markers with turquoise edges are for true periods longer than 3000 days. Point sizes are proportional to SNR.

rendering the filtering process ineffective, we examined the number of data points within subharmonic and harmonic ranges from 2 to 10.

At least half of the data for all groups lay within detected-to-true amplitude and period ratios of 2. With each consecutive detected-to-true ratio, the additional number of data decreases. For the CBD group, the detected-to-true amplitude and period ratio plot is presented in Figure 5, while for the groups of UBD, CPL, and UPL, the same plots are presented in Figures 9, 10 and 11 in respective orders. We focused on a ratio value of 2, where the data clustered around the 1:1 region, and a ratio value of 3, which includes harmonics and subharmonics.

Table 1 summarizes the simulated eclipsing binary sample sizes and detection counts across the four groups. Each group contains over 60,000 simulated systems, ensuring comparability across groups. Detection rates were highest for the CBD and UBD, ranging from 2.92% to 5.03%, while CPL and UPL groups exhibited significantly lower detection rates, with a maximum of 0.10%. The median circumbinary mass across the entire sam-

ple is $56.6^{+16.5}_{-23.4} M_J$. Additionally, the detection rates of CBD systems are approximately 30% higher than in UBD systems. Furthermore, the results indicate that BDs are about 50 times more likely to be detected using the ETV method than Jupiter-like planets in the mass range of 1–13 M_J , highlighting the sensitivity of this technique when applied to TESS data.

The total binary mass in the detected sample spans from 0.2 M_\odot to 5.6 M_\odot , with a median value of $0.54^{+0.68}_{-0.25} M_\odot$. The corresponding binary periods range from 0.75 to 33.1 days, with a median period of $3.1^{+3.0}_{-1.4}$ days. The detected sample is skewed toward lower binary masses and shorter binary periods, as these conditions lead to higher ETV amplitudes and a greater number of timing measurements within the observational baseline.

The TESS magnitudes of the recovered systems range from 4 to 14 mag. The number of both simulated and recovered eclipsing binaries increases with decreasing system brightness. In contrast, the number of recovered systems peaks where timing uncertainties remain low enough for detections, with a median TESS magnitude

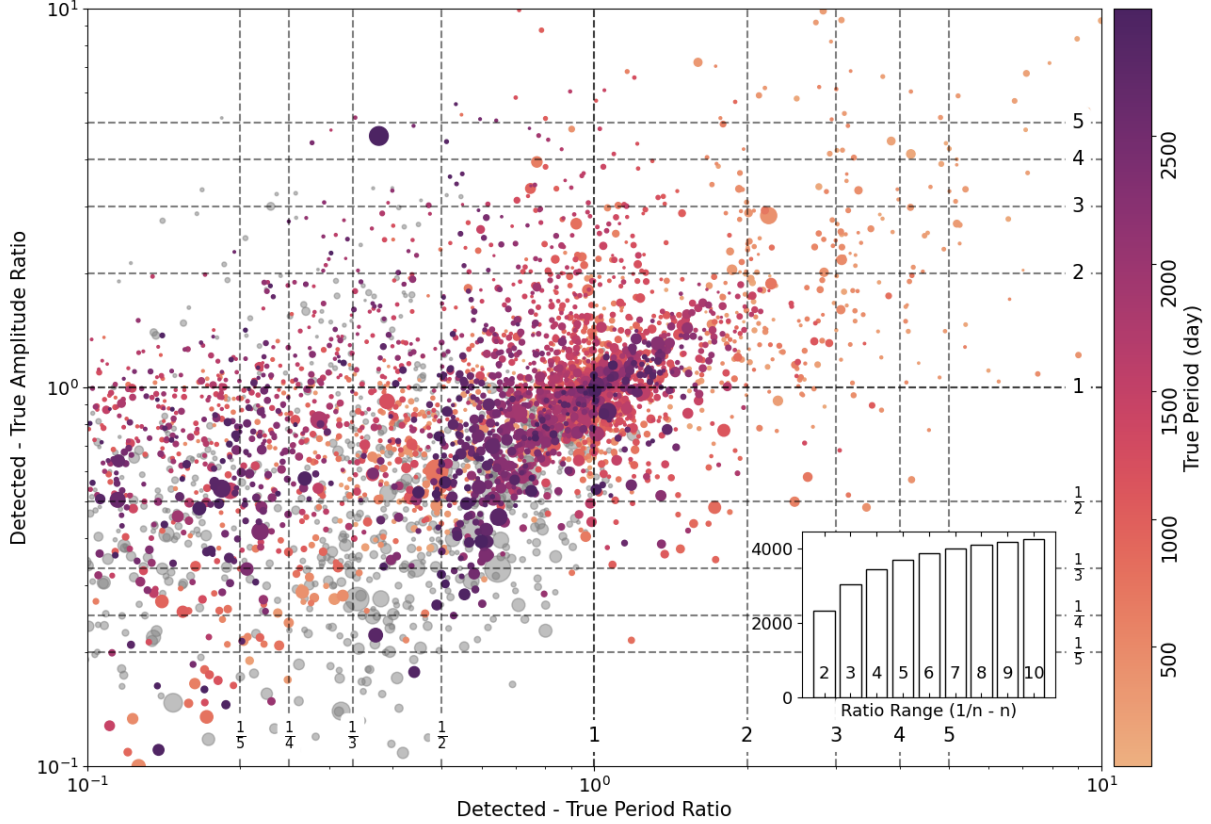


Figure 5. Similar to Figure 4 but for the SNR, FAP and detected-to-binary period ratio thresholds-applied coplanar & brown dwarf (CBD) group, zoomed to 0.1 - 10 ratio range on both axes. The color scale represents true periods, with darker points indicating longer periods. Grey markers are for true periods longer than 3000 days. Point sizes are proportional to SNR. Lower-right: The subplot represents the data within the $1/n - n$ ratio range on both axes. There are 2317 data points within the $1/2 - 2$ ratio and 3022 points within the $1/3 - 3$ ratio ranges, including true periods longer than 3000 days (grey).

of $12.82^{+0.87}_{-1.79}$ mag. The ETV uncertainties of the recovered sample span 0.4 s to 240 s, with a median value of $16.4^{+20.7}_{-9.7}$ s. Figure 6 shows these distributions for the entire sample of eclipsing binaries and the recovered systems.

The distribution of recovered systems across the sky reveals a concentration near the Galactic plane, particularly in regions neighboring the TESS CVZ on both hemispheres (cyan or warmer-colored regions in Figure 2). While the CVZ benefits from long-term observational coverage, it is not the most densely populated region for recoveries due to the lower number of eclipsing binaries compared to the Galactic plane. Additionally, most recovered systems are found in regions with fewer than 20 observed TESS sectors, outnumbering those with more than 20 sectors by a factor of ten. However, TESS data for sources near the Galactic plane are expected to suffer from significant contamination due to the large pixel sizes. As a result, real detections in these regions are more likely to be either bright sources, where the impact of contamination is reduced, or sys-

tems located at higher Galactic latitudes compared to our recovered sample.

Table 1. Simulated eclipsing binary sample and detection counts across CBD, UBD, CPL, and UPL groups. The $1/n - n$ values represent the thresholds for detected-to-true period and amplitude ratios, with detections defined as data within these limits. We used thresholds of 2 and 3. Additional detection thresholds for SNR, FAP, and detected-to-binary period ratio were also applied. Labels: C = coplanar orbit, U = uniform inclination, PL = planet mass, BD = brown dwarf mass.

	CBD	UBD	CPL	UPL
Total Number	60102	59933	65636	65541
Detection	2317	1751	52	38
$1/2 - 2$	(3.86%)	(2.92%)	(0.08%)	(0.06%)
Detection	3022	2364	66	45
$1/3 - 3$	(5.03%)	(3.94%)	(0.10%)	(0.07%)

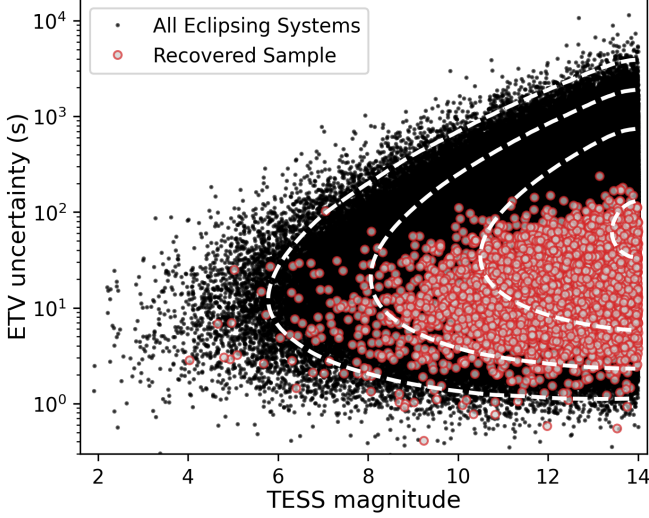


Figure 6. TESS magnitude versus ETV uncertainty (σ_{ETV}) for the entire sample of eclipsing binaries (black points) and the recovered sample (red circles). The dashed contours highlight density variations in the entire sample. The recovered systems are concentrated in regions with lower timing uncertainties, while the overall distribution shows increasing uncertainty with decreasing brightness.

3.4. Occurrence Rates

In our ETV modeling of the target sample, assuming a given binary mass, we calculated the hypothetical circumbinary masses corresponding to the peak frequencies in the periodograms. For six systems, these masses were found to be below $0.08 M_{\odot}$. Among them, variations in five systems, excluding TIC 350297040, are likely due to out-of-eclipse variations, apsidal motion, or sampling effects. However, for TIC 350297040, we do not yet have a definitive explanation for the detected variation. Consequently, we proceed with occurrence rate calculations under two scenarios. One assumes no confirmed planetary detections in the sample ($k = 0$) to provide an upper limit, and the other includes TIC 350297040 as a candidate system ($k = 1$). For all scenarios, we consider the coplanar cases only.

For both scenarios, we use the relation:

$$f = \frac{k}{R \cdot N} \quad (3)$$

where f is the occurrence rate, k is the number of detections, R is the recovery rate, and N is the total number of systems analyzed.

In the first scenario, with $k = 0$, the upper limit on f is calculated using binomial statistics. The probability of observing zero detections in N systems is:

$$P(k = 0|f) = (1 - f)^N \quad (4)$$

which at a confidence level of α gives an upper limit to f as,

$$f_{\text{upper}} = 1 - (1 - \alpha)^{1/N} \quad (5)$$

For $N = 152$ targets, we find $f_{\text{upper}} \approx 0.020124$ for $\alpha = 0.9545$. Correcting for the recovery rate of the CBD group, $R = 5.03\%$, the true upper limit on the occurrence rate can be calculated as,

$$f_{\text{upper, corr}} = \frac{f_{\text{upper}}}{R} \quad (6)$$

which implies that the occurrence rate of detectable brown dwarfs in the sample is constrained to be less than 40.01% at a 2σ confidence level. In the second scenario, assuming $k = 1$, the occurrence rate of circumbinary brown dwarfs is estimated at 13.08%.

For planetary-mass objects ($< 13 M_J$) and a recovery rate of the CPL group ($R = 0.0010$), the calculated occurrence rate upper limit (f) exceeds 1, indicating that detections based solely on TESS data are not sufficiently sensitive for such masses. This reflects the low recovery rate and observational limitations of TESS. Complementary datasets or improved techniques are needed to enhance sensitivity to planetary-mass objects around binary systems.

4. SUMMARY AND DISCUSSION

We investigated the eclipse timing variations (ETVs) of detached eclipsing binaries observed by TESS to identify potential circumbinary companions. Our target selection was based on the TEBC, focusing on detached binaries that allow for precise timing measurements. We modeled their light curves and ETVs using `allesfitter` and performed Lomb-Scargle analyses on 152 systems. Among these, 26 exhibited significant periodicities in their ETVs, though for some, the observed variations could be attributed to out-of-eclipse modulations. Assuming that the observed ETV signals originate from the LiTE due to circumbinary companions, we estimated their hypothetical masses and found that six systems could host objects in the brown dwarf mass range. One system, TIC 350297040, shows an ETV signal that may be due to a circumbinary brown dwarf, as there is currently no other indication of an alternative source for the variation. However, further detailed investigation is required to confirm this scenario. The observed ETV signals are likely caused by stellar variability, apsidal motion, or sampling effects for the remaining five systems.

To further assess the detectability of circumbinary brown dwarfs and planets, we conducted simulations incorporating various parameters related to binary star properties and potential circumbinary objects. The synthetic ETVs used in these simulations were generated

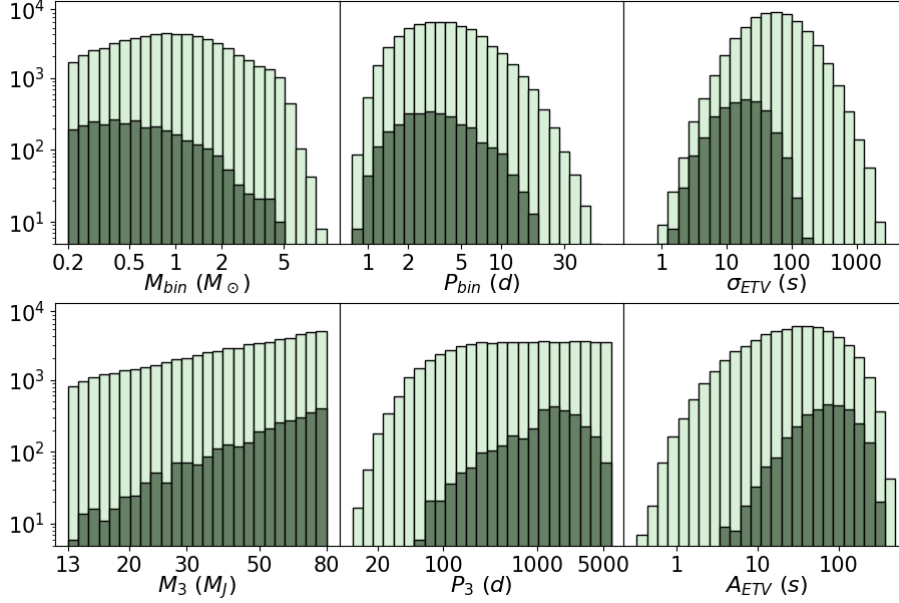


Figure 7. The distributions of parameters for coplanar & brown dwarf (CBD) group. The light colors are for all the samples where the binary is eclipsing, while the dark colors are for the sample where circumbinary objects detected between 1/3 - 3 range for amplitude and period ratios. Note that both axes for all distributions are on a logarithmic scale.

using noise properties derived from our TESS ETV modeling (see Figure 6). These simulations allowed us to calculate the recovery rates of the ETV method, yielding approximately 5% for brown dwarfs and 0.1% for Jupiter-like planets.

The detection of simulated circumbinary objects in our study reveals trends that align with theoretical expectations while providing quantitative insights into the parameter space where detections are most likely. Systems with smaller binary masses (M_{bin}) are more likely to yield detectable signals, allowing the circumbinary object to induce a more pronounced wobble in the binary. On the other hand, shorter binary periods are favored because they ensure a sufficient number of eclipses can be observed within the TESS data. Similarly, systems with smaller ETV uncertainties (σ_{ETV}) are more sensitive to detecting circumbinary companions. For circumbinary objects, higher masses (M_3) and longer periods (P_3) are more frequently associated with detections, even when the periods exceed the observational time span of the data. The peak periods detected for circumbinary objects are between 1000 and 2000 days. The corresponding distributions for the CBD group are shown in Figure 7, which compares the entire eclipsing binary sample (light colors) to the detected circumbinary objects (dark colors). The overall features are common for UBD, CPL, and UPL groups, while the detected sample size is considerably smaller for the latter two. The only notable difference for PL groups is that the M_3 parameter for the detected sample becomes uniform

for masses larger than $5M_J$, an effect of the planet mass function of Mordasini (2018).

TESS observations may be crucial in filling this gap and identifying new long-period circumbinary companions. Notably, the ETV planet associated with the longest binary period is Kepler-1660 (Getley et al. 2017), whose detection relied on dynamical interactions between the stars and the planet rather than the LiTE mechanism explored in this study.

Figure 8 illustrates our recovered ETV sample in the circumbinary period vs. binary period space, highlighting how different detection methods populate this region. A clear separation emerges between transiting and radial velocity detections, which cluster around binaries with periods of 10 days or more. In contrast, current ETV detections are primarily found around shorter-period binaries. Our simulated sample bridges this gap, overlapping more with transiting and RV-detected planets, suggesting potential confirmation of ETV signals using these complementary methods. However, the sensitivity of the ETV method biases our recovered sample toward shorter binary periods ($3.09^{+3.04} - 1.37$ days) and longer circumbinary periods ($1404^{+1361} - 953$ days), a region currently devoid of known circumbinary substellar objects. The figure also provides insight into survey completeness, comparing our recovered sample with known circumbinary planets and simulated populations. While our survey spans binary periods of 1.5 to 13.7 days, simulations suggest greater sensitivity at shorter binary periods, indicating that increasing

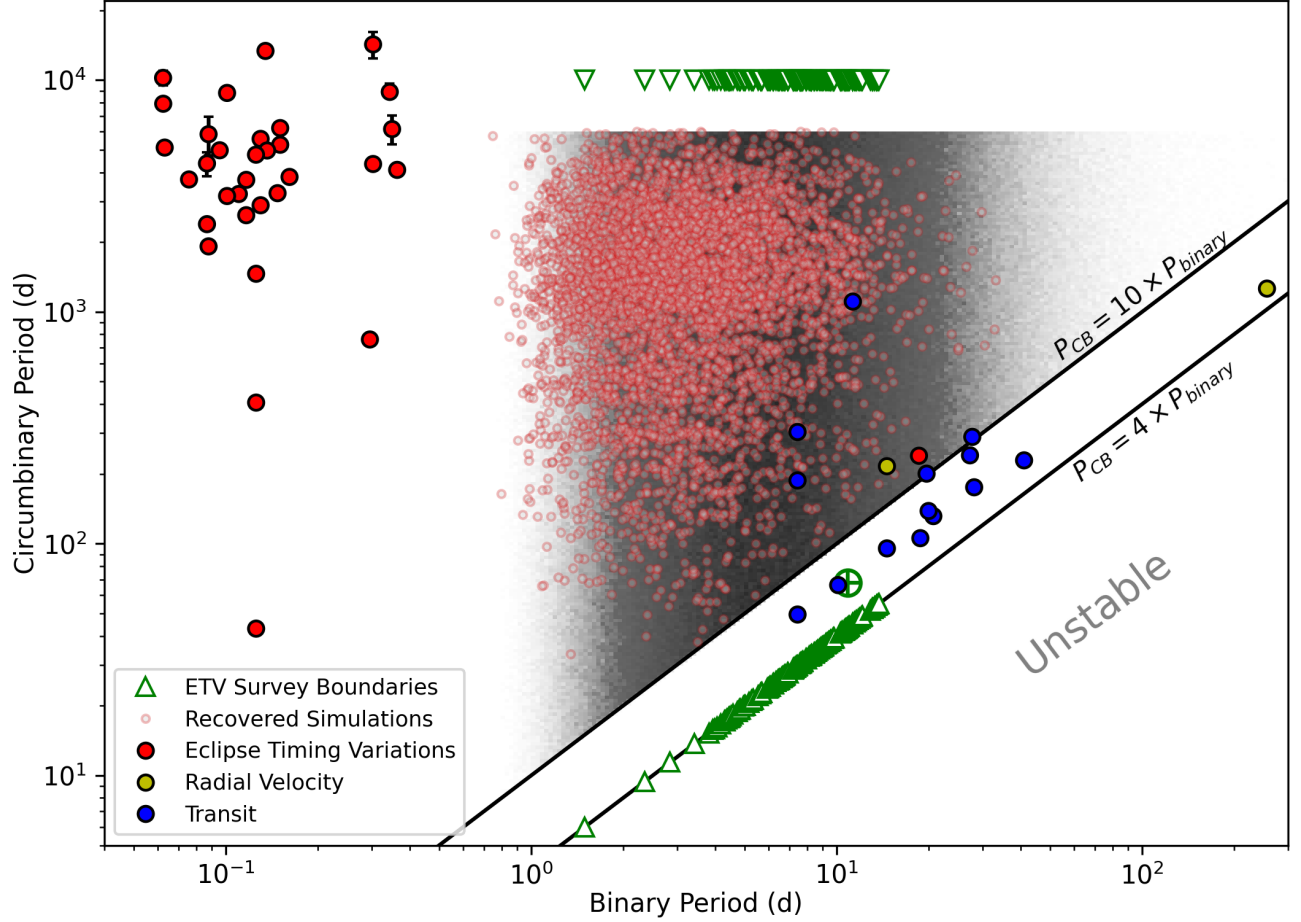


Figure 8. Recovered sample from our ETV simulations (small red markers) overlaid on the known circumbinary planet population, color-coded by detection method (see legend). The gray shading represents the full simulated population. The black lines indicate circumbinary period constraints at $4 \times P_{\text{binary}}$ and $10 \times P_{\text{binary}}$, with orbits below $4 \times P_{\text{binary}}$ considered dynamically unstable. Green triangles mark the Lomb-Scargle period search range in our ETV survey of 152 targets, where each triangle corresponds to the search range for a given binary period. TIC 350297040 is highlighted with a green circle and plus signs, aligning well with known transiting circumbinary planets, though further analysis is required to confirm its nature.

survey density in this range would improve detectability. TESS observations may be crucial for identifying long-period circumbinary companions and refining occurrence rate estimates, though expanding the survey is essential to capture the diverse nature of these systems. The ETV planet associated with the longest binary period is Kepler-1660 (Getley et al. 2017), detected via dynamical interactions rather than the LiTE mechanism explored here.

Circumbinary disks tend to be misaligned when the binary period exceeds approximately 30 days (Czekala et al. 2019), suggesting that circumbinary objects in such systems are also more likely to have misaligned orbits. This period threshold is close to the upper limit of binary periods in our simulations (33.1 days for recovered samples), indicating that our simulations are more representative of the coplanar scenario rather than a uniform or randomly misaligned inclination distribution.

While the coplanar case is more favorable for ETV detections, our results show that the ETV method remains efficient enough to recover misaligned circumbinary objects, albeit with a lower detection rate (coplanar brown dwarfs are 30% more likely to be detected via ETVs than uniformly inclined counterparts). However, there is an inherent degeneracy in determining inclination when relying solely on ETVs. By incorporating complementary methods, such as radial velocity measurements, the underlying inclination distribution of circumbinary objects can be constrained in sufficiently large surveys.

Using the recovery rates, we estimated an upper limit on the occurrence rate of circumbinary brown dwarfs and found that it should not exceed approximately 40% at a two-sigma confidence level. This limit is notably higher than the $<6.5\%$ constraint placed by the BEBOP radial velocity survey (Martin et al. 2019) over a similar mass and period range. If we instead assume a single de-

tection, our estimated occurrence rate is 13.08%, which is approximately twice the upper limit set by BEBOP. Due to the low recovery rate for planetary-mass objects, we were unable to place meaningful constraints on their occurrence rates. Although the photometric precision of TESS introduces some limitations, its extensive dataset, which potentially includes $\sim 300,000$ eclipsing binaries (Kruse et al. 2021), provides a valuable resource for large-scale ETV studies like this one. This work lays the foundation for future searches and further investigations into the population of circumbinary objects.

The majority of current circumbinary substellar discoveries via eclipse timing variations (ETVs) are found around short-period (< 0.5 d) evolved eclipsing binaries, where the primary stars are either subdwarf B (sdB) stars or white dwarfs (WDs) with low-mass main sequence companions. The progenitors of these primaries are estimated to be $\lesssim 2 M_{\odot}$ (Arancibia-Rojas et al. 2024) for sdBs and up to $8 M_{\odot}$ for WDs (Cunningham et al. 2024). In our ETV simulations, we identified 78,589 binaries with primary and secondary masses within the expected progenitor range of currently known ETV hosts ($1 M_{\odot} < M_1 < 8 M_{\odot}$, $M_2 < 1 M_{\odot}$), yet we successfully recovered only 651 systems, yielding a recovery rate of just 0.78%.

The formation pathways of circumbinary substellar companions around PCEBs remain an open question, with two competing scenarios: first-generation objects that formed within the protoplanetary disk of the young binary and second-generation objects that formed within a circumbinary disk during or after the common-envelope phase (Zorotovic & Schreiber 2013). Despite their relative rarity, evolved post-common envelope binaries frequently host circumbinary substellar companions, implying that if these objects are of first-generation origin, their progenitor binaries must have hosted them in significant numbers. Given the intrinsically low recovery rate of 0.78% in our simulations, even a single discovery of a circumbinary substellar companion around a PCEB progenitor in TESS data would strongly favor the first-generation scenario. Therefore, a systematic search for these objects across a larger sample of progenitor binaries is crucial to constrain their formation mechanisms.

While we were not able to put constraints on the occurrence rates of Jupiter-like planets, our findings highlight the potential of ETVs in detecting massive circumbinary companions, with the smallest mass detected from synthetic ETV data being $1.6 M_J$ at an orbital period of 1860 d, demonstrating the method’s reach under optimistic conditions. We plan to expand our target sample and incorporate additional data from complementary surveys to improve detection limits and extend our sensitivity to lower-mass objects. While the substellar companions detectable via ETVs are typically massive, their gravitational influence can play a crucial role in shaping the orbital evolution of terrestrial siblings and even provide stable environments for habitable exomoons. These results emphasize the need for larger datasets and multi-method approaches to fully uncover the diversity of planets in circumbinary systems, potentially revealing new worlds that challenge our understanding of planetary formation and habitability.

This paper includes data collected with the TESS mission, obtained from the MAST data archive at the Space Telescope Science Institute (STScI). Funding for the TESS mission is provided by the NASA Explorer Program. STScI is operated by the Association of Universities for Research in Astronomy, Inc., under NASA contract NAS 5–26555. This work has made use of data from the European Space Agency (ESA) mission *Gaia* (<https://www.cosmos.esa.int/gaia>), processed by the *Gaia* Data Processing and Analysis Consortium (DPAC, <https://www.cosmos.esa.int/web/gaia/dpac/consortium>). Funding for the DPAC has been provided by national institutions, in particular, the institutions participating in the *Gaia* Multilateral Agreement.

Software: Allesfitter (Günther & Daylan 2021, 2019), Astropy (Astropy Collaboration et al. 2013, 2018, 2022), Corner (Foreman-Mackey 2016), Matplotlib (Hunter 2007), NumPy (Harris et al. 2020), Pandas (Wes McKinney 2010; pandas development team 2024), Rebound (Rein & Liu 2012), SciPy (Virtanen et al. 2020), TESS-Point (Burke et al. 2020)

APPENDIX

Table 2. Results for Lomb-Scargle analyses of the ETVs of Our Targets. The table lists the TIC IDs, detected periods, amplitudes, and false alarm probabilities (FAPs) corresponding to the strongest peak in the Lomb-Scargle periodogram.

TESS ID	Period (day)	Amplitude (min)	False Alarm Probability
TIC 260502102	2592.8	8.58	1.94×10^{-112}

TESS ID	Period (day)	Amplitude (min)	False Alarm Probability
TIC 373915220	590.5	3.41	5.23×10^{-27}
TIC 237944385	2117.5	4.04	6.20×10^{-20}

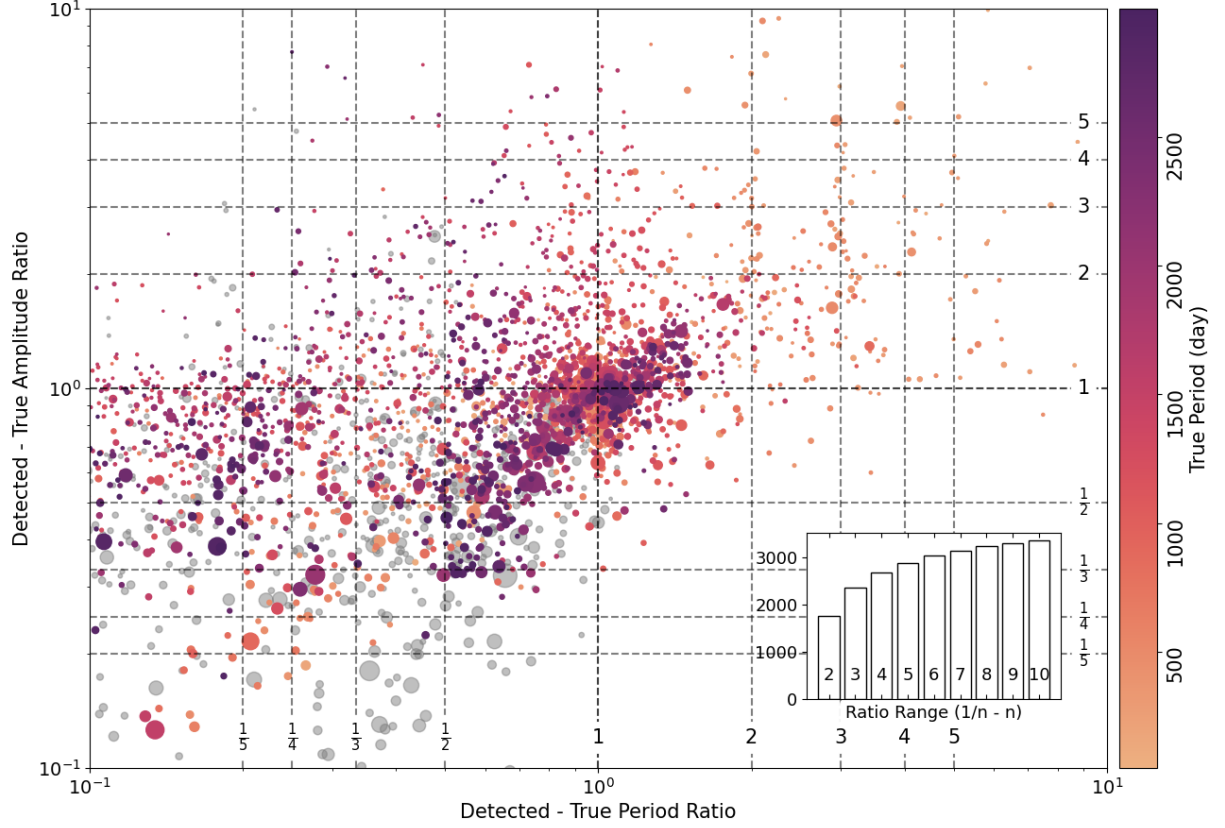


Figure 9. Similar to Figure 5 but for uniform inclination & brown dwarf (UBD) group.

TESS ID	Period (day)	Amplitude (min)	False Alarm Probability	TESS ID	Period (day)	Amplitude (min)	False Alarm Probability
TIC 167692429	327.6	46.01	1.20×10^{-12}	TIC 159720778	48.1	0.68	9.86×10^{-02}
TIC 26542657	1140.6	31.75	1.01×10^{-11}	TIC 366072761	30.6	0.91	0.11
TIC 102929927	2535.9	6.29	1.74×10^{-11}	TIC 197570458	30.9	3.14	0.12
TIC 198537349	283.2	0.78	5.12×10^{-08}	TIC 336405638	45.0	0.47	0.13
TIC 142979644	535.0	0.33	2.49×10^{-07}	TIC 250196734	368.2	8.42	0.16
TIC 300161053	1428.8	44.28	1.65×10^{-04}	TIC 356641568	211.8	1.64	0.18
TIC 184298625	413.4	2.37	4.71×10^{-04}	TIC 388529207	29.5	0.87	0.18
TIC 278988794	740.5	3.44	5.96×10^{-04}	TIC 91542943	31.2	0.55	0.19
TIC 3816260	67.2	0.15	1.03×10^{-03}	TIC 317507345	21.1	1.82	0.22
TIC 166090445	544.1	0.46	1.27×10^{-03}	TIC 11756637	17.5	0.34	0.25
TIC 230063769	38.3	0.48	2.39×10^{-03}	TIC 272086869	1431.5	3.69	0.25
TIC 407584737	30.9	2.56	1.94×10^{-02}	TIC 371706494	60.3	0.23	0.27
TIC 180412528	78.1	0.30	1.97×10^{-02}	TIC 332334202	121.6	0.37	0.27
TIC 323301918	235.9	7.06	2.05×10^{-02}	TIC 149990841	152.2	1.77	0.29
TIC 140659980	406.6	0.62	2.80×10^{-02}	TIC 339185356	32.3	0.43	0.30
TIC 118313102	41.3	1.00	3.80×10^{-02}	TIC 18914916	55.1	0.29	0.31
TIC 303427297	34.9	0.80	4.35×10^{-02}	TIC 373328406	38.5	1.15	0.31
TIC 270648838	158.3	0.14	4.47×10^{-02}	TIC 255548311	20.9	0.55	0.32
TIC 219707463	23.4	0.31	4.67×10^{-02}	TIC 235009317	35.7	2.04	0.32
TIC 350297040	67.7	0.15	7.06×10^{-02}	TIC 148611095	1774.5	4.05	0.37
TIC 103452621	159.9	1.91	7.95×10^{-02}	TIC 232185093	19.5	0.37	0.39
TIC 56128191	52.7	1.64	8.89×10^{-02}	TIC 300871545	46.8	0.26	0.41

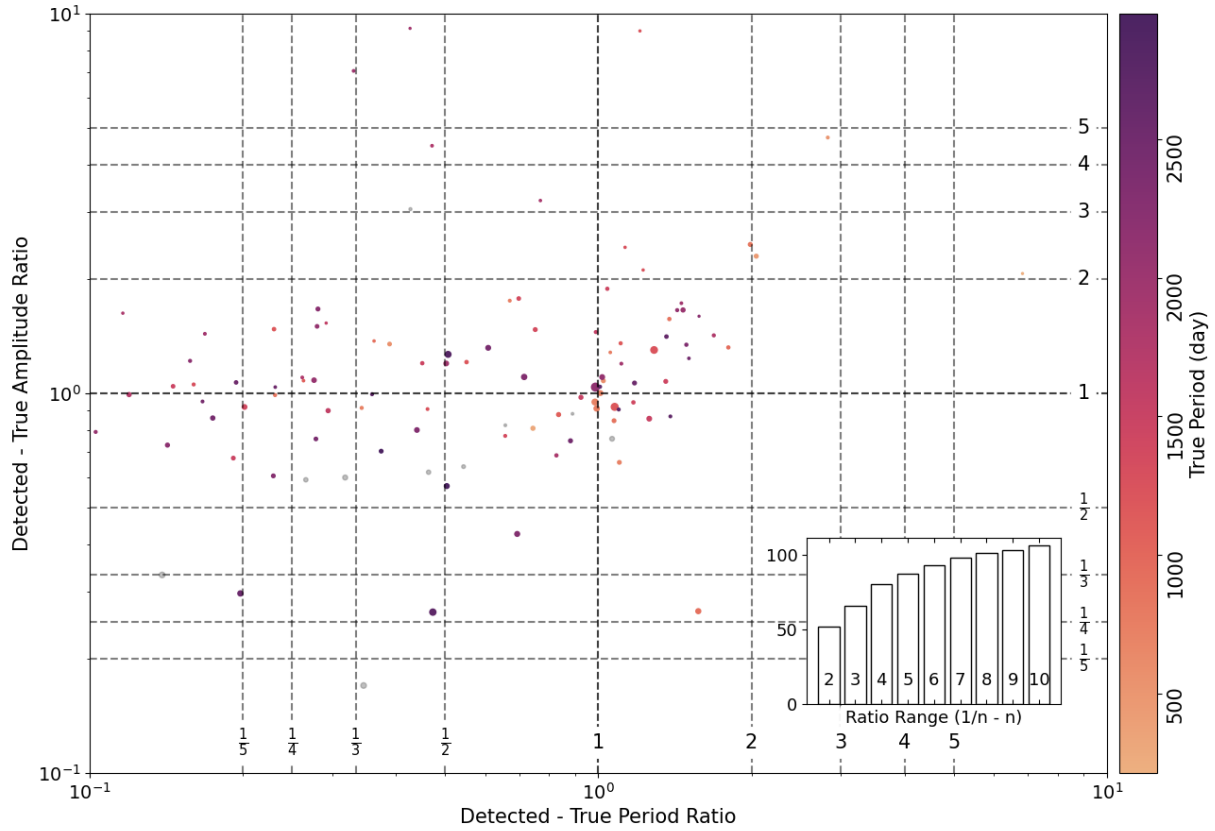


Figure 10. Similar to Figure 5 but for coplanar & planet (CPL) group.

TESS ID	Period (day)	Amplitude (min)	False Alarm Probability	TESS ID	Period (day)	Amplitude (min)	False Alarm Probability
TIC 258918831	30.0	0.72	0.43	TIC 236387002	36.8	0.37	0.77
TIC 229616860	89.4	0.49	0.47	TIC 173038281	17.3	0.57	0.77
TIC 379215982	386.3	15.72	0.50	TIC 103605167	40.1	0.03	0.78
TIC 124199788	17.0	0.45	0.51	TIC 1400770435	55.0	1.09	0.81
TIC 139721086	340.5	0.08	0.55	TIC 274129522	261.8	0.45	0.82
TIC 238197709	156.1	3.88	0.59	TIC 101395259	30.7	2.63	0.83
TIC 233390838	281.3	1.77	0.59	TIC 349518145	68.4	0.96	0.84
TIC 470085533	53.8	0.27	0.59	TIC 364120439	49.8	1.05	0.86
TIC 66355834	115.9	0.22	0.61	TIC 238626074	20.7	0.57	0.86
TIC 288434781	30.3	0.14	0.61	TIC 192071095	68.0	0.83	0.87
TIC 350479101	101.8	0.25	0.62	TIC 360661624	49.4	2.72	0.89
TIC 170344769	48.7	1.49	0.63	TIC 9433212	31.5	0.49	0.89
TIC 159047480	79.4	1.63	0.65	TIC 261335113	56.1	0.21	0.89
TIC 203001339	116.8	0.42	0.67	TIC 352110251	184.8	12.62	0.90
TIC 310785613	25.9	1.10	0.70	TIC 349154435	202.2	0.63	0.90
TIC 260504147	39.8	0.10	0.70	TIC 297899564	63.3	0.08	0.92
TIC 256327585	56.5	2.55	0.71	TIC 191933664	48.2	0.42	0.92
TIC 309619055	134.4	4.97	0.75	TIC 135050395	27.3	0.50	0.92
TIC 167201539	70.5	0.37	0.75	TIC 148612685	44.9	0.16	0.92
TIC 92349924	36.9	1.89	0.75	TIC 27915909	52.4	1.31	0.92
TIC 382188882	20.2	1.50	0.75	TIC 38937499	16.2	0.90	0.93
TIC 350743714	65.9	1.25	0.76	TIC 305466446	37.0	1.14	0.93

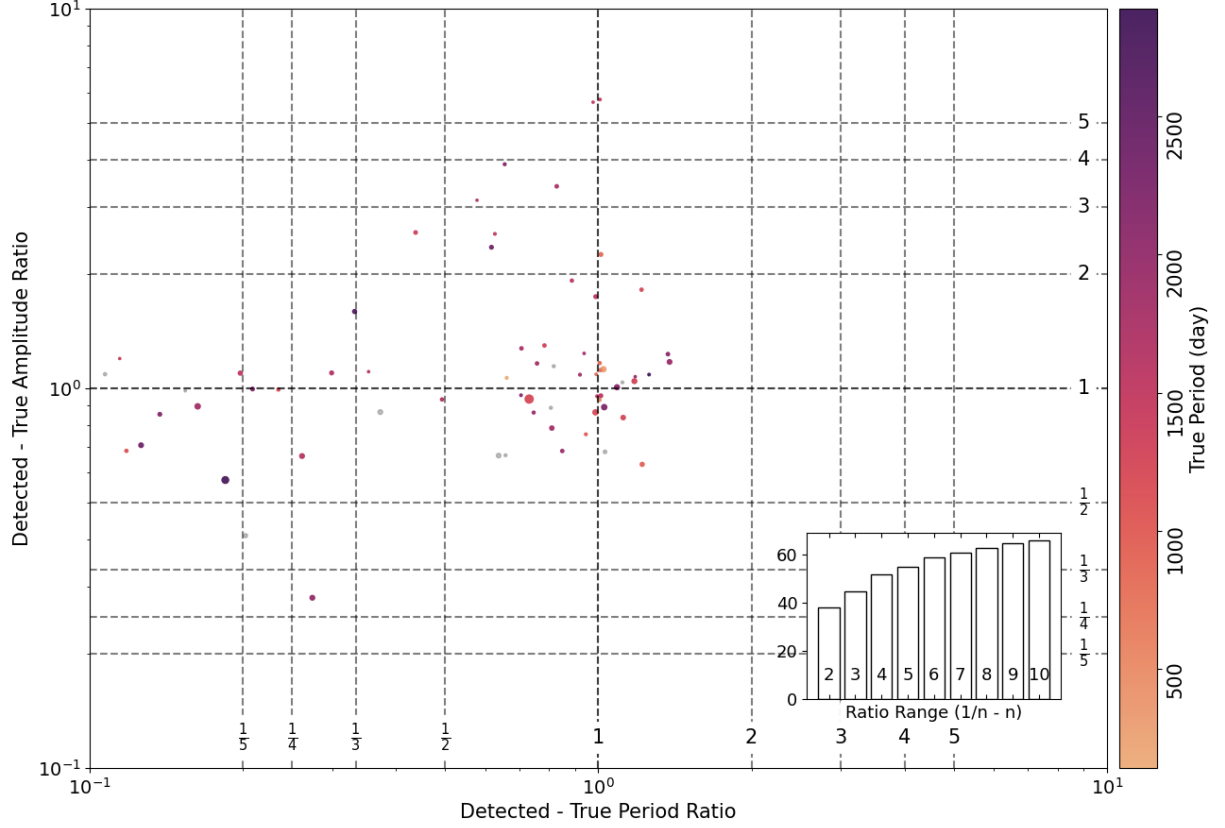


Figure 11. Similar to Figure 5 but for uniform inclination & planet (UPL) group.

TESS ID	Period (day)	Amplitude (min)	False Alarm Probability	TESS ID	Period (day)	Amplitude (min)	False Alarm Probability
TIC 293480903	30.7	0.44	0.93	TIC 277683130	25.7	4.03	1.00
TIC 39818458	15.2	0.51	0.94	TIC 456033358	51.0	0.25	1.00
TIC 382517745	191.1	0.18	0.94	TIC 182469311	41.9	3.10	1.00
TIC 279949020	78.7	0.30	0.95	TIC 162035117	53.0	1.56	1.00
TIC 114819301	39.6	1.06	0.95	TIC 365070128	29.9	1.24	1.00
TIC 77951245	43.8	1.68	0.96	TIC 279454212	369.8	10.46	1.00
TIC 229808144	455.3	3.10	0.96	TIC 22390773	45.9	0.22	1.00
TIC 424992973	34.8	0.22	0.97	TIC 341193555	39.7	0.30	1.00
TIC 143117999	363.5	1918.62	0.97	TIC 424719589	30.6	0.02	1.00
TIC 1883519478	30.6	0.04	0.98	TIC 356015361	49.9	11.65	1.00
TIC 233722938	236.3	0.23	0.98	TIC 369283035	45.6	0.49	1.00
TIC 147975720	11.4	0.25	0.98	TIC 22818693	35.7	0.05	1.00
TIC 459894730	52.3	0.69	0.98	TIC 320524751	61.1	0.18	1.00
TIC 168312820	27.7	1.99	0.99	TIC 18028547	30.3	0.09	1.00
TIC 115920747	42.3	0.42	0.99	TIC 124095230	43.0	1.10	1.00
TIC 164554097	76.4	0.58	0.99	TIC 142852841	13.7	0.26	1.00
TIC 302384263	32.8	0.40	0.99	TIC 180943676	33.7	0.45	1.00
TIC 137549183	46.6	0.23	0.99	TIC 167795859	43.3	1.23	1.00
TIC 188590080	26.6	1.00	1.00	TIC 144000467	229.0	16.98	1.00
TIC 402112785	67.7	3.39	1.00	TIC 27006880	44.8	1.02	1.00
TIC 274575202	38.5	0.18	1.00	TIC 260269456	161.8	0.04	1.00
TIC 123573766	27.2	1.19	1.00	TIC 445074203	17.8	1.27	1.00

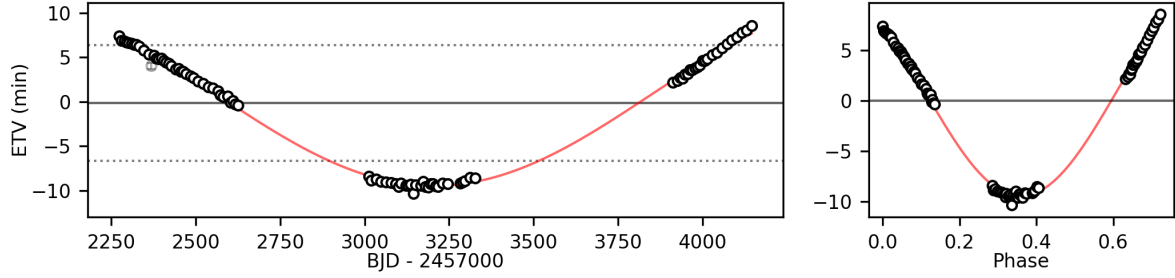


Figure 12. Eclipse Timing Variations (ETVs) of TIC 260502102. The left panel displays the timing data as white circles, with excluded data shown in gray circles or triangles if they fall outside the plot range. The red curve represents the model corresponding to the strongest peak in the Lomb-Scargle periodogram. The right panel presents the phase-folded ETVs with an arbitrary phase start value for visualization.

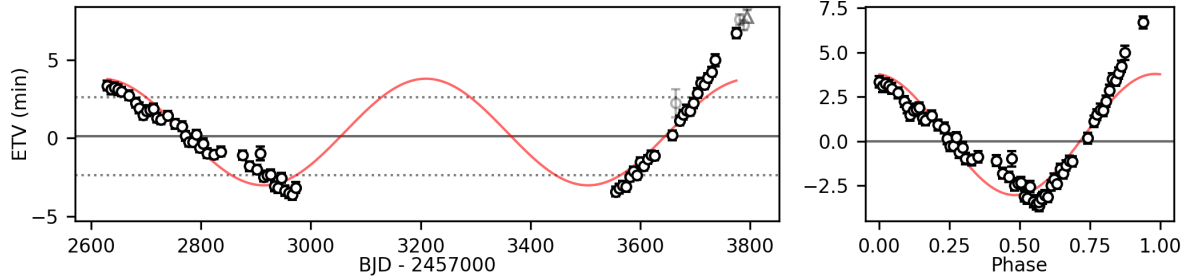


Figure 13. ETV of TIC 373915220

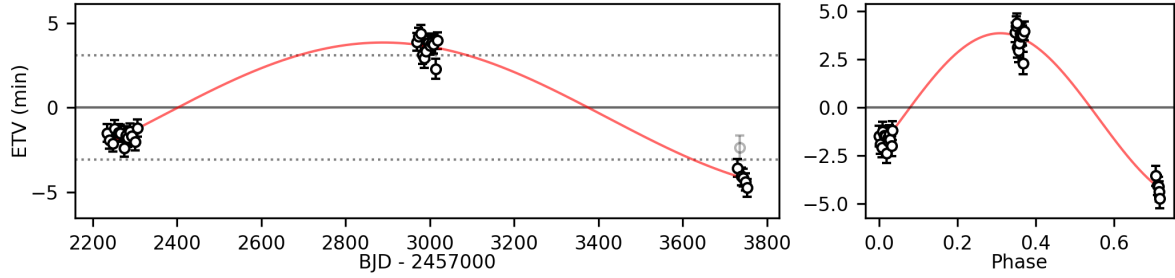


Figure 14. ETV of TIC 237944385

TESS ID	Period (day)	Amplitude (min)	False Alarm Probability				
TIC 278784173	6.0	0.22	1.00	TIC 417734853	56.6	0.09	1.00
TIC 261656371	34.0	0.05	1.00	TIC 356015357	52.3	0.03	1.00
TIC 273697554	1457.9	3.82	1.00	TIC 161577376	92.8	0.58	1.00
TIC 220523550	916.9	25.06	1.00	TIC 102169275	247.1	51.79	1.00
TIC 365203184	21.3	1.74	1.00	TIC 72534221	29.9	1.40	1.00
TIC 160328766	41.3	0.11	1.00	TIC 98658304	24.1	0.86	1.00
TIC 308991822	63.2	0.11	1.00	TIC 296780789	73.4	4.23	1.00
TIC 39018208	26.6	0.73	1.00	TIC 49534600	32.0	1.88	1.00

REFERENCES

Arancibia-Rojas, E., Zorotovic, M., Vučković, M., et al.

Armstrong, D. J., Osborn, H. P., Brown, D. J. A., et al.

2024, MNRAS, 527, 11184, doi: [10.1093/mnras/stad3891](https://doi.org/10.1093/mnras/stad3891)

2014, MNRAS, 444, 1873, doi: [10.1093/mnras/stu1570](https://doi.org/10.1093/mnras/stu1570)

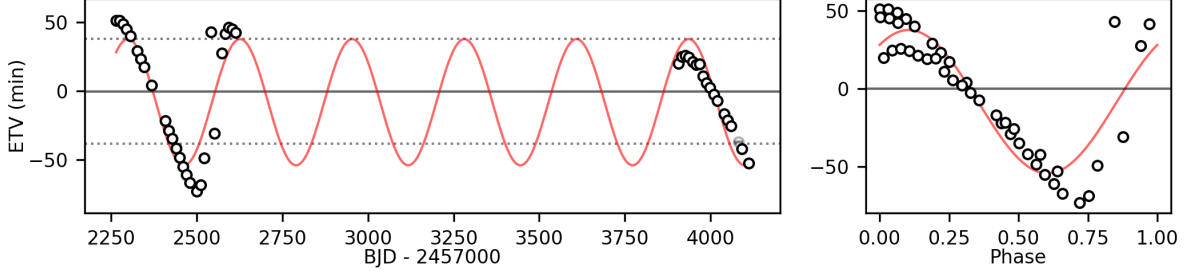


Figure 15. ETV of TIC 167692429

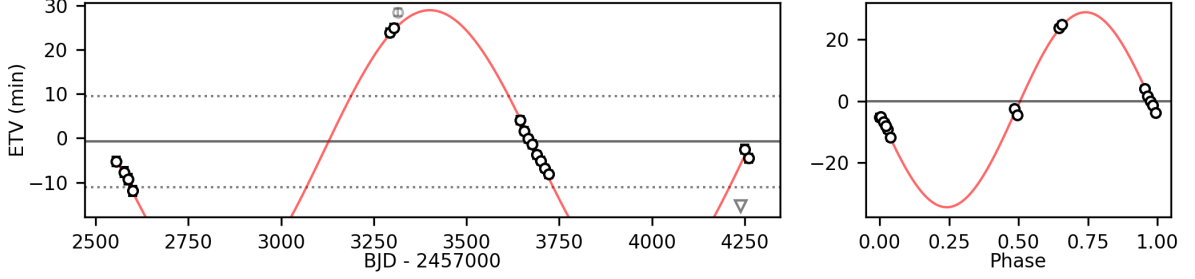


Figure 16. ETV of TIC 26542657

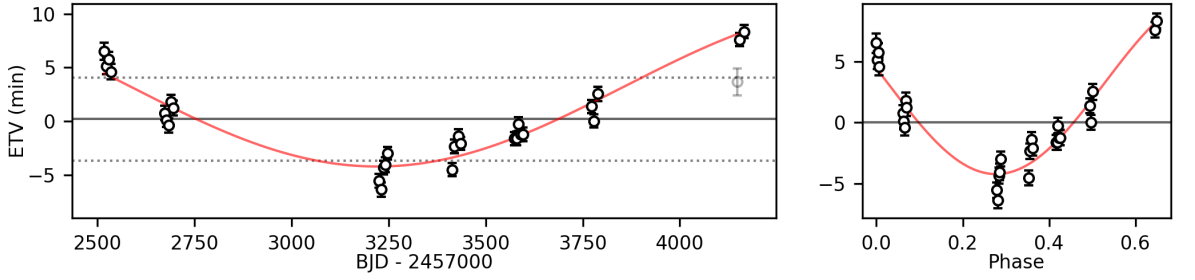


Figure 17. ETV of TIC 102929927

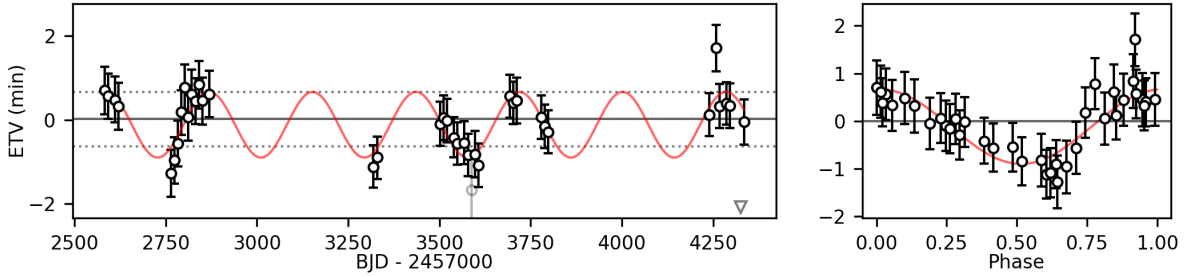


Figure 18. ETV of TIC 198537349

Astropy Collaboration, Robitaille, T. P., Tollerud, E. J., et al. 2013, *A&A*, 558, A33, doi: [10.1051/0004-6361/201322068](https://doi.org/10.1051/0004-6361/201322068)

Astropy Collaboration, Price-Whelan, A. M., Sipőcz, B. M., et al. 2018, *AJ*, 156, 123, doi: [10.3847/1538-3881/aabc4f](https://doi.org/10.3847/1538-3881/aabc4f)

Astropy Collaboration, Price-Whelan, A. M., Lim, P. L., et al. 2022, *ApJ*, 935, 167, doi: [10.3847/1538-4357/ac7c74](https://doi.org/10.3847/1538-4357/ac7c74)

Baştürk, Ö., Esmer, E. M., Demir, E., & Selam, S. O. 2023, *Bulletin de la Societe Royale des Sciences de Liege*, 92, 11197, doi: [10.25518/0037-9565.11197](https://doi.org/10.25518/0037-9565.11197)

Bear, E., & Soker, N. 2014, *MNRAS*, 444, 1698, doi: [10.1093/mnras/stu1529](https://doi.org/10.1093/mnras/stu1529)

Benedict, G. F., & Harrison, T. E. 2017, *AJ*, 153, 258, doi: [10.3847/1538-3881/aa6d59](https://doi.org/10.3847/1538-3881/aa6d59)

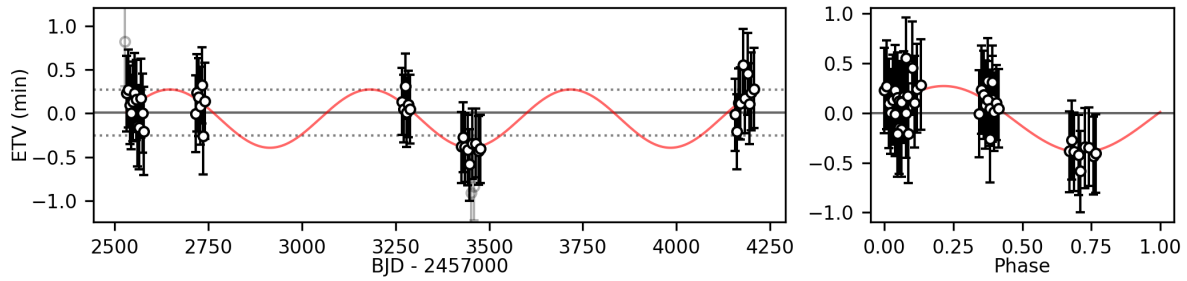


Figure 19. ETV of TIC 142979644

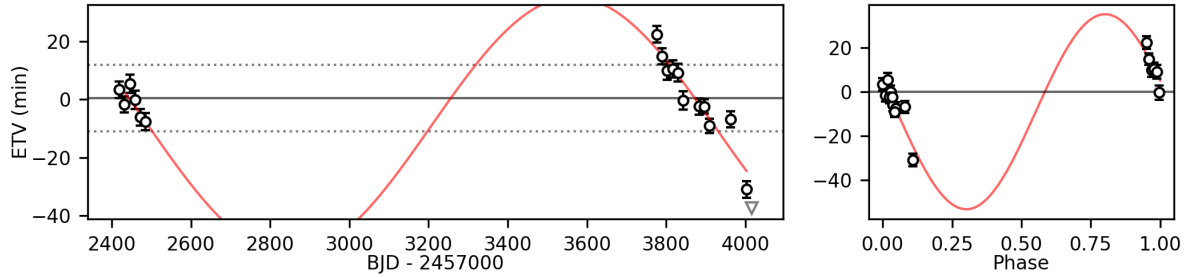


Figure 20. ETV of TIC 300161053

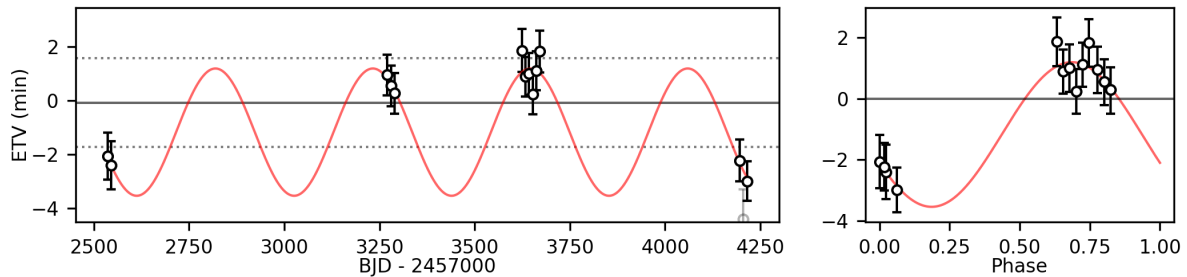


Figure 21. ETV of TIC 184298625

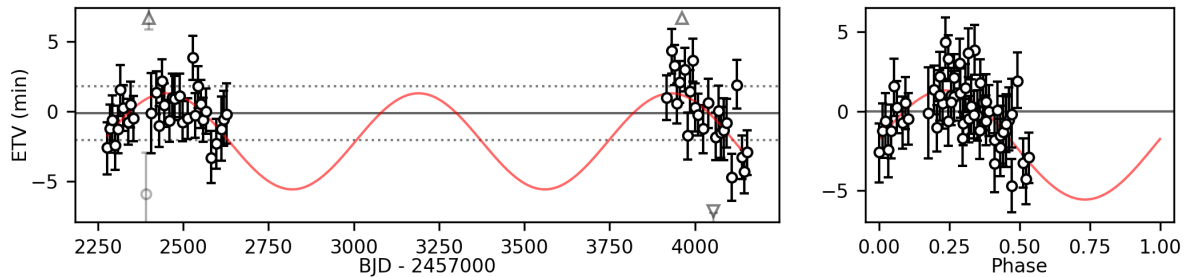


Figure 22. ETV of TIC 278988794

Bennett, D. P., Rhie, S. H., Udalski, A., et al. 2016, *AJ*, 152, 125, doi: [10.3847/0004-6256/152/5/125](https://doi.org/10.3847/0004-6256/152/5/125)

Bonavita, M., Desidera, S., Thalmann, C., et al. 2016, *A&A*, 593, A38, doi: [10.1051/0004-6361/201628231](https://doi.org/10.1051/0004-6361/201628231)

Borkovits, T., Hajdu, T., Sztakovics, J., et al. 2016, *MNRAS*, 455, 4136, doi: [10.1093/mnras/stv2530](https://doi.org/10.1093/mnras/stv2530)

Borkovits, T., Rappaport, S., Hajdu, T., & Sztakovics, J. 2015, *MNRAS*, 448, 946, doi: [10.1093/mnras/stv015](https://doi.org/10.1093/mnras/stv015)

Borkovits, T., Rappaport, S. A., Hajdu, T., et al. 2020, *MNRAS*, 493, 5005, doi: [10.1093/mnras/staa495](https://doi.org/10.1093/mnras/staa495)

Bours, M. C. P., Marsh, T. R., Parsons, S. G., et al. 2016, *MNRAS*, 460, 3873, doi: [10.1093/mnras/stw1203](https://doi.org/10.1093/mnras/stw1203)

Burke, C. J., Levine, A., Fausnaugh, M., et al. 2020, TESS-Point: High precision TESS pointing tool, Astrophysics Source Code Library.

<http://ascl.net/2003.001>

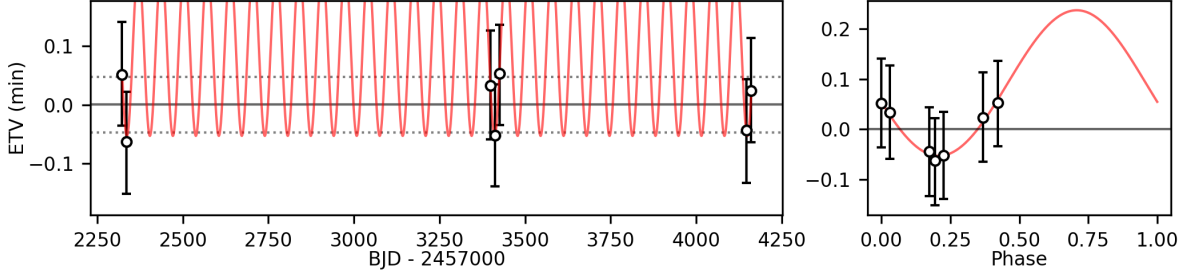


Figure 23. ETV of TIC 3816260

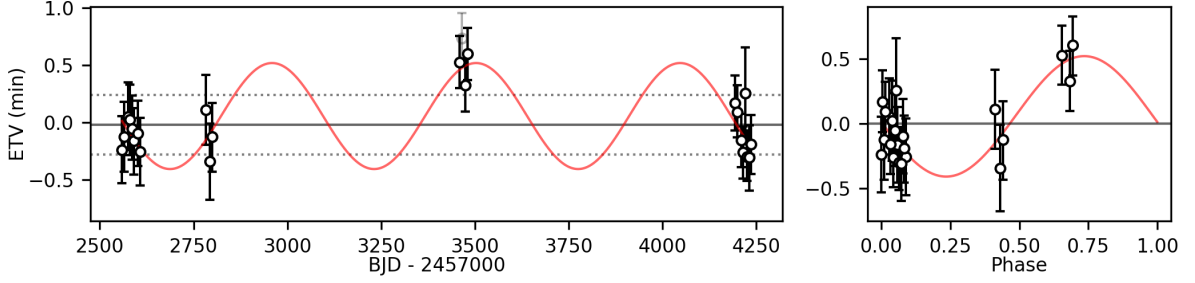


Figure 24. ETV of TIC 166090445

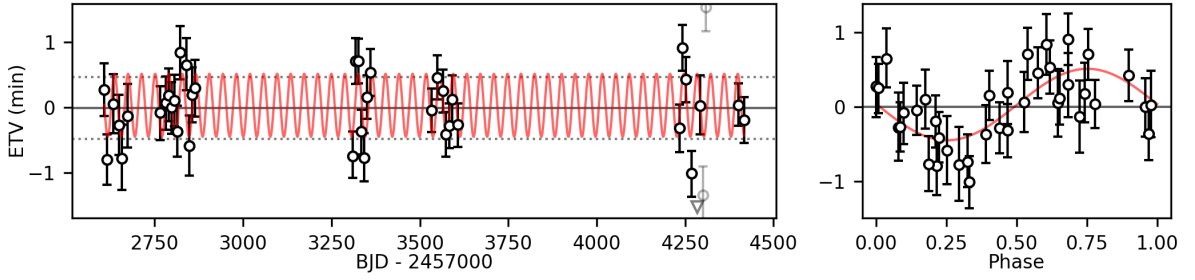


Figure 25. ETV of TIC 230063769

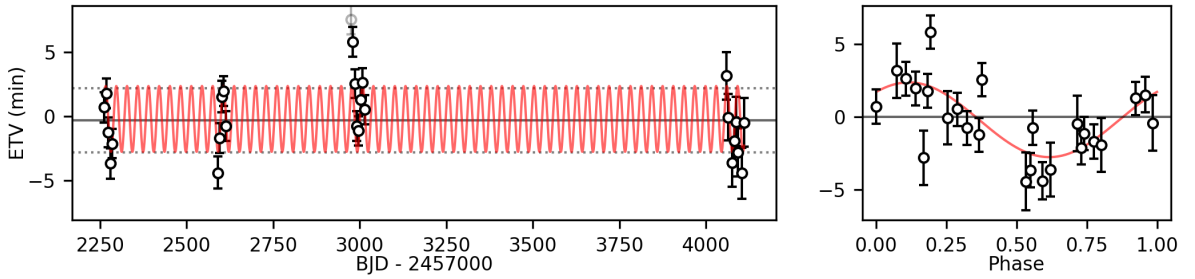


Figure 26. ETV of TIC 407584737

Cañas, C. I., Mahadevan, S., Bender, C. F., et al. 2022, *AJ*, 163, 89, doi: [10.3847/1538-3881/ac415f](https://doi.org/10.3847/1538-3881/ac415f)

Chabrier, G. 2003, *PASP*, 115, 763, doi: [10.1086/376392](https://doi.org/10.1086/376392)

Chavez, C. E., Georgakarakos, N., Prodan, S., et al. 2015, *MNRAS*, 446, 1283, doi: [10.1093/mnras/stu2142](https://doi.org/10.1093/mnras/stu2142)

Chen, C., Lubow, S. H., Martin, R. G., & Nixon, C. J. 2023, *MNRAS*, 521, 5033, doi: [10.1093/mnras/stad739](https://doi.org/10.1093/mnras/stad739)

Chen, C., Martin, R. G., Lubow, S. H., & Nixon, C. J. 2024, *ApJL*, 961, L5, doi: [10.3847/2041-8213/ad17c5](https://doi.org/10.3847/2041-8213/ad17c5)

Coleman, G. A. L. 2024, *MNRAS*, 530, 630, doi: [10.1093/mnras/stae903](https://doi.org/10.1093/mnras/stae903)

Coleman, G. A. L., Nelson, R. P., Triaud, A. H. M. J., & Standing, M. R. 2024, *MNRAS*, 527, 414, doi: [10.1093/mnras/stad3216](https://doi.org/10.1093/mnras/stad3216)

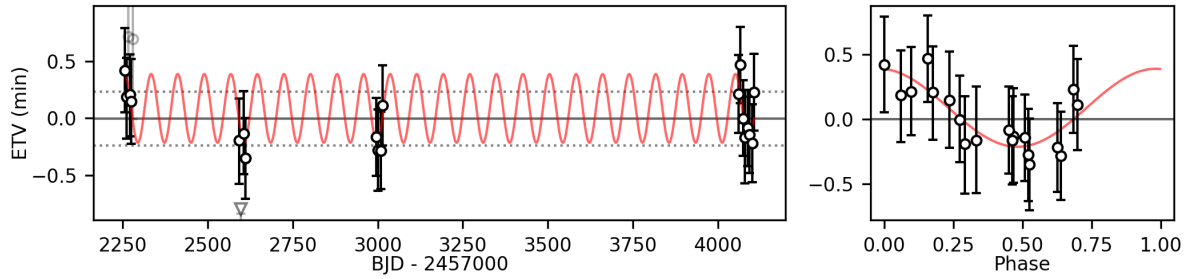


Figure 27. ETV of TIC 180412528

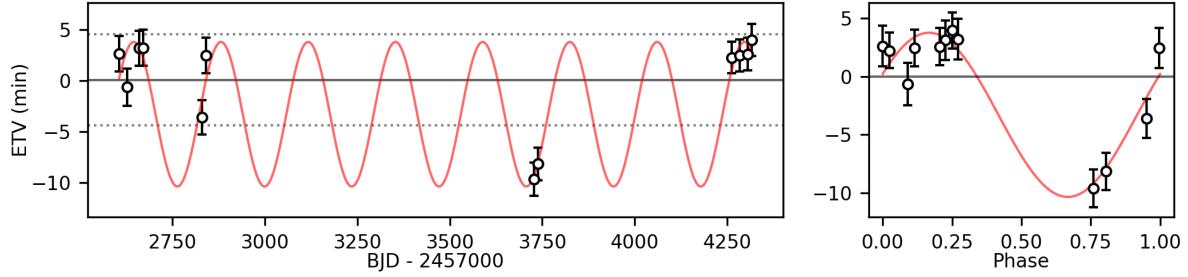


Figure 28. ETV of TIC 323301918

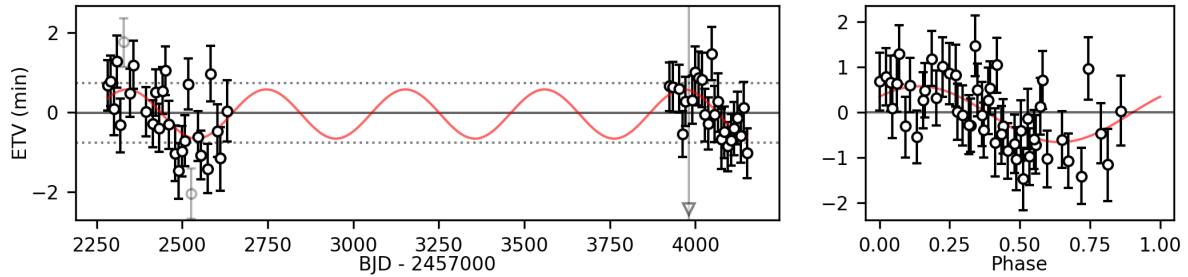


Figure 29. ETV of TIC 140659980

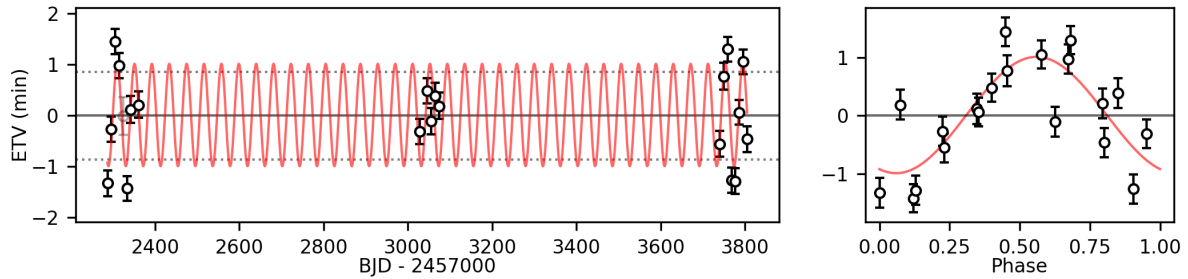


Figure 30. ETV of TIC 118313102

Correia, A. C. M., Boué, G., & Laskar, J. 2016, *Celestial Mechanics and Dynamical Astronomy*, 126, 189, doi: [10.1007/s10569-016-9709-9](https://doi.org/10.1007/s10569-016-9709-9)

Cunningham, T., Tremblay, P.-E., & W. O'Brien, M. 2024, *MNRAS*, 527, 3602, doi: [10.1093/mnras/stad3275](https://doi.org/10.1093/mnras/stad3275)

Czekala, I., Chiang, E., Andrews, S. M., et al. 2019, *ApJ*, 883, 22, doi: [10.3847/1538-4357/ab287b](https://doi.org/10.3847/1538-4357/ab287b)

Deeg, H. J. 2020, *Galaxies*, 9, 1, doi: [10.3390/galaxies9010001](https://doi.org/10.3390/galaxies9010001)

Deeg, H. J., & Tingley, B. 2017, *A&A*, 599, A93, doi: [10.1051/0004-6361/201629350](https://doi.org/10.1051/0004-6361/201629350)

Esmer, E. M., Baştürk, Ö., Hinse, T. C., Selam, S. O., & Correia, A. C. M. 2021, *A&A*, 648, A85, doi: [10.1051/0004-6361/202038640](https://doi.org/10.1051/0004-6361/202038640)

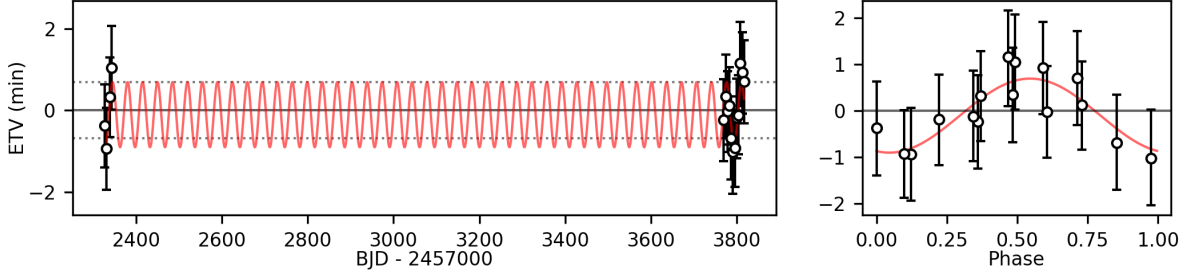


Figure 31. ETV of TIC 303427297

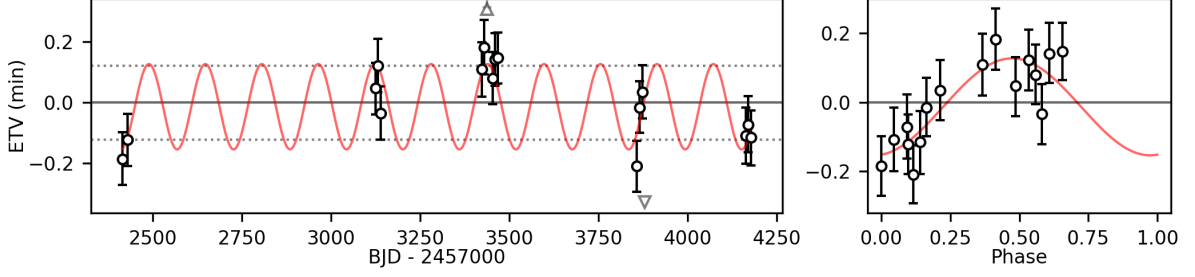


Figure 32. ETV of TIC 270648838

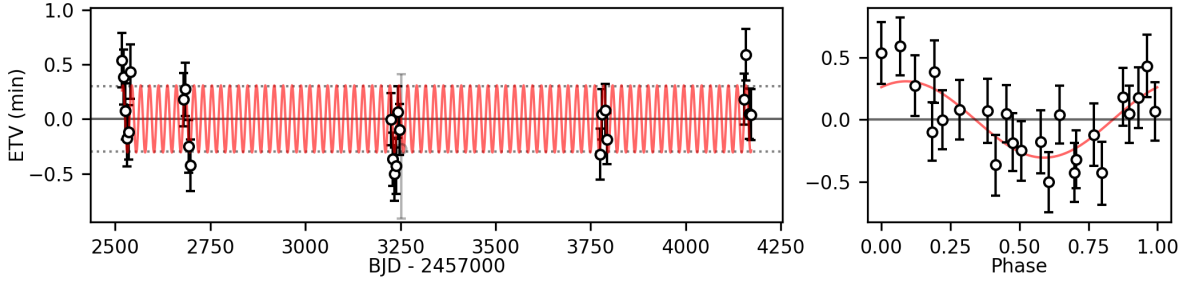


Figure 33. ETV of TIC 219707463

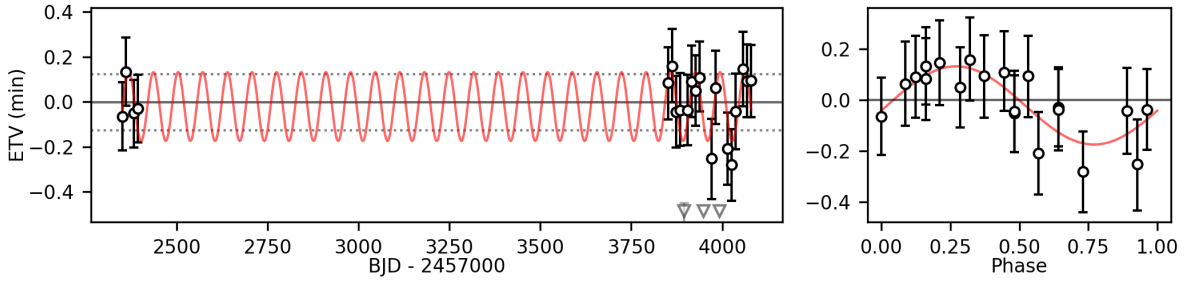


Figure 34. ETV of TIC 350297040

Esmer, E. M., Baştürk, Ö., & Selam, S. O. 2023, MNRAS, 525, 6050, doi: [10.1093/mnras/stad2648](https://doi.org/10.1093/mnras/stad2648)

Esmer, E. M., Baştürk, Ö., Selam, S. O., et al. 2024, Contributions of the Astronomical Observatory Skalnaté Pleso, 54, 228, doi: [10.31577/caosp.2024.54.2.228](https://doi.org/10.31577/caosp.2024.54.2.228)

Esmer, E. M., Baştürk, Ö., Selam, S. O., & Aliş, S. 2022, MNRAS, 511, 5207, doi: [10.1093/mnras/stac357](https://doi.org/10.1093/mnras/stac357)

Fleming, D. P., Barnes, R., Graham, D. E., Luger, R., & Quinn, T. R. 2018, ApJ, 858, 86, doi: [10.3847/1538-4357/aabd38](https://doi.org/10.3847/1538-4357/aabd38)

Foreman-Mackey, D. 2016, Journal of Open Source Software, 1, 24, doi: [10.21105/joss.00024](https://doi.org/10.21105/joss.00024)

Foucart, F., & Lai, D. 2013, ApJ, 764, 106, doi: [10.1088/0004-637X/764/1/106](https://doi.org/10.1088/0004-637X/764/1/106)

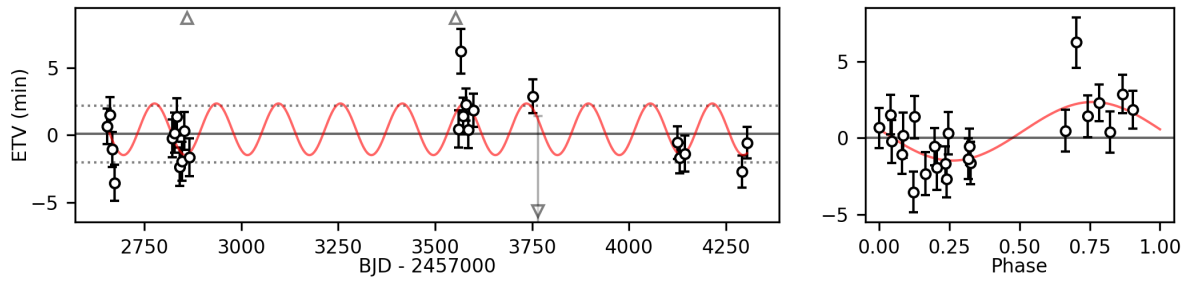


Figure 35. ETV of TIC 103452621

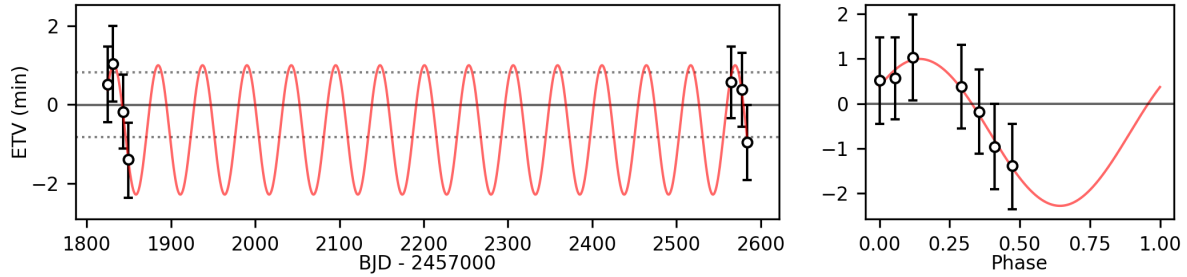


Figure 36. ETV of TIC 56128191

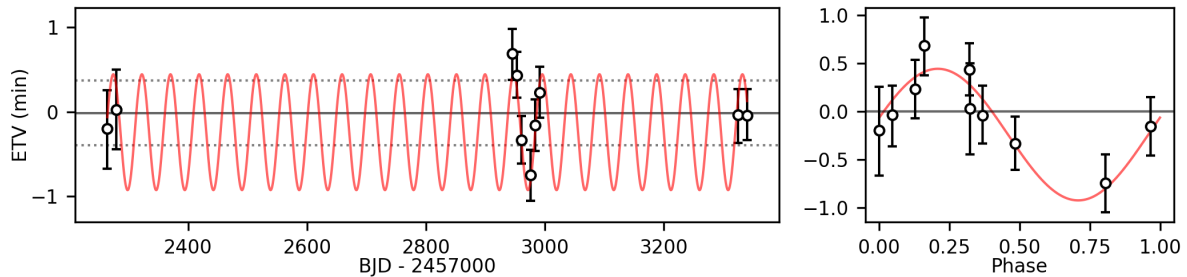


Figure 37. ETV of TIC 159720778

Gaia Collaboration, Prusti, T., de Bruijne, J. H. J., et al. 2016, *A&A*, 595, A1, doi: [10.1051/0004-6361/201629272](https://doi.org/10.1051/0004-6361/201629272)

Gaia Collaboration, Vallenari, A., Brown, A. G. A., et al. 2023, *A&A*, 674, A1, doi: [10.1051/0004-6361/202243940](https://doi.org/10.1051/0004-6361/202243940)

Getley, A. K., Carter, B., King, R., & O'Toole, S. 2017, *MNRAS*, 468, 2932, doi: [10.1093/mnras/stx604](https://doi.org/10.1093/mnras/stx604)

—. 2021, *MNRAS*, 504, 4291, doi: [10.1093/mnras/stab1207](https://doi.org/10.1093/mnras/stab1207)

Gorda, S. Y., & Svechnikov, M. A. 1998, *Astronomy Reports*, 42, 793

Graham, D. E., Fleming, D. P., & Barnes, R. 2021, *A&A*, 650, A178, doi: [10.1051/0004-6361/202038940](https://doi.org/10.1051/0004-6361/202038940)

Guerrero, N. M., Seager, S., Huang, C. X., et al. 2021, *ApJS*, 254, 39, doi: [10.3847/1538-4365/abefel](https://doi.org/10.3847/1538-4365/abefel)

Günther, M. N., & Daylan, T. 2019, *Allesfitter: Flexible Star and Exoplanet Inference From Photometry and Radial Velocity*, *Astrophysics Source Code Library*. <http://ascl.net/1903.003>

—. 2021, *ApJS*, 254, 13, doi: [10.3847/1538-4365/abe70e](https://doi.org/10.3847/1538-4365/abe70e)

Haghighipour, N., & Kaltenegger, L. 2013, *ApJ*, 777, 166, doi: [10.1088/0004-637X/777/2/166](https://doi.org/10.1088/0004-637X/777/2/166)

Hamers, A. S., Perets, H. B., & Portegies Zwart, S. F. 2016, *MNRAS*, 455, 3180, doi: [10.1093/mnras/stv2447](https://doi.org/10.1093/mnras/stv2447)

Harris, C. R., Millman, K. J., van der Walt, S. J., et al. 2020, *Nature*, 585, 357, doi: [10.1038/s41586-020-2649-2](https://doi.org/10.1038/s41586-020-2649-2)

Hunter, J. D. 2007, *Computing in Science & Engineering*, 9, 90, doi: [10.1109/MCSE.2007.55](https://doi.org/10.1109/MCSE.2007.55)

Kane, S. R., & Hinkel, N. R. 2013, *ApJ*, 762, 7, doi: [10.1088/0004-637X/762/1/7](https://doi.org/10.1088/0004-637X/762/1/7)

Kostov, V. B., Orosz, J. A., Welsh, W. F., et al. 2016, *ApJ*, 827, 86, doi: [10.3847/0004-637X/827/1/86](https://doi.org/10.3847/0004-637X/827/1/86)

Kruse, E., Powell, B., Kostov, V., Schnittman, J., & Quintana, E. 2021, in *Posters from the TESS Science Conference II (TSC2)*, 163, doi: [10.5281/zenodo.5131355](https://doi.org/10.5281/zenodo.5131355)

Lomb, N. R. 1976, *Ap&SS*, 39, 447, doi: [10.1007/BF00648343](https://doi.org/10.1007/BF00648343)

Marcadon, F., & Prša, A. 2024, *arXiv e-prints*, arXiv:2403.07694, doi: [10.48550/arXiv.2403.07694](https://doi.org/10.48550/arXiv.2403.07694)

- Martin, D. V., & Triaud, A. H. M. J. 2014, *A&A*, 570, A91, doi: [10.1051/0004-6361/201323112](https://doi.org/10.1051/0004-6361/201323112)
- Martin, D. V., Triaud, A. H. M. J., Udry, S., et al. 2019, *A&A*, 624, A68, doi: [10.1051/0004-6361/201833669](https://doi.org/10.1051/0004-6361/201833669)
- Marzari, F., & Thebault, P. 2019, *Galaxies*, 7, 84, doi: [10.3390/galaxies7040084](https://doi.org/10.3390/galaxies7040084)
- Mikulášek, Z., Chrástina, M., Liška, J., et al. 2014, *Contributions of the Astronomical Observatory Skalnaté Pleso*, 43, 382
- Mitnyan, T., Borkovits, T., Czavalinga, D. R., et al. 2024, *A&A*, 685, A43, doi: [10.1051/0004-6361/202348909](https://doi.org/10.1051/0004-6361/202348909)
- Moharana, A., Helminiak, K. G., Marcadon, F., et al. 2024, *MNRAS*, 527, 53, doi: [10.1093/mnras/stad3117](https://doi.org/10.1093/mnras/stad3117)
- Mordasini, C. 2018, *Planetary Population Synthesis* (Cham: Springer International Publishing), 2425–2474, doi: [10.1007/978-3-319-55333-7_143](https://doi.org/10.1007/978-3-319-55333-7_143)
- Orosz, J. A., Welsh, W. F., Haghighipour, N., et al. 2019, *AJ*, 157, 174, doi: [10.3847/1538-3881/ab0ca0](https://doi.org/10.3847/1538-3881/ab0ca0)
- pandas development team, T. 2024, *pandas-dev/pandas: Pandas, v2.2.1*, Zenodo, doi: [10.5281/zenodo.10697587](https://doi.org/10.5281/zenodo.10697587)
- Papageorgiou, A., Catelan, M., Christopoulou, P.-E., Drake, A. J., & Djorgovski, S. G. 2021, *MNRAS*, 503, 2979, doi: [10.1093/mnras/stab646](https://doi.org/10.1093/mnras/stab646)
- Pribulla, T., Vaňko, M., Ammler-von Eiff, M., et al. 2012, *Astronomische Nachrichten*, 333, 754, doi: [10.1002/asna.201211722](https://doi.org/10.1002/asna.201211722)
- Prša, A., Kochoska, A., Conroy, K. E., et al. 2022, *ApJS*, 258, 16, doi: [10.3847/1538-4365/ac324a](https://doi.org/10.3847/1538-4365/ac324a)
- Quarles, B., Satyal, S., Kostov, V., Kaib, N., & Haghighipour, N. 2018, *ApJ*, 856, 150, doi: [10.3847/1538-4357/aab264](https://doi.org/10.3847/1538-4357/aab264)
- Rein, H., & Liu, S. F. 2012, *A&A*, 537, A128, doi: [10.1051/0004-6361/201118085](https://doi.org/10.1051/0004-6361/201118085)
- Rein, H., & Spiegel, D. S. 2015, *MNRAS*, 446, 1424, doi: [10.1093/mnras/stu2164](https://doi.org/10.1093/mnras/stu2164)
- Ricker, G. R., Winn, J. N., Vanderspek, R., et al. 2015, *Journal of Astronomical Telescopes, Instruments, and Systems*, 1, 014003, doi: [10.1117/1.JATIS.1.1.014003](https://doi.org/10.1117/1.JATIS.1.1.014003)
- Scargle, J. D. 1982, *ApJ*, 263, 835, doi: [10.1086/160554](https://doi.org/10.1086/160554)
- Schanche, N., Collier Cameron, A., Almenara, J. M., et al. 2019, *MNRAS*, 488, 4905, doi: [10.1093/mnras/stz2064](https://doi.org/10.1093/mnras/stz2064)
- Simonetti, P., Vladilo, G., Silva, L., & Sozzetti, A. 2020, *ApJ*, 903, 141, doi: [10.3847/1538-4357/abc074](https://doi.org/10.3847/1538-4357/abc074)
- Standing, M. R., Sairam, L., Martin, D. V., et al. 2023, *Nature Astronomy*, 7, 702, doi: [10.1038/s41550-023-01948-4](https://doi.org/10.1038/s41550-023-01948-4)
- Sybilski, P., Konacki, M., & Kozłowski, S. K. 2010, *MNRAS*, 405, 657, doi: [10.1111/j.1365-2966.2010.16490.x](https://doi.org/10.1111/j.1365-2966.2010.16490.x)
- Tofflemire, B. M., Kraus, A. L., Mann, A. W., et al. 2023, *AJ*, 165, 46, doi: [10.3847/1538-3881/aca60f](https://doi.org/10.3847/1538-3881/aca60f)
- VanderPlas, J. T. 2018, *ApJS*, 236, 16, doi: [10.3847/1538-4365/aab766](https://doi.org/10.3847/1538-4365/aab766)
- Virtanen, P., Gommers, R., Oliphant, T. E., et al. 2020, *Nature Methods*, 17, 261, doi: [10.1038/s41592-019-0686-2](https://doi.org/10.1038/s41592-019-0686-2)
- von Boetticher, A., Triaud, A. H. M. J., Queloz, D., et al. 2017, *A&A*, 604, L6, doi: [10.1051/0004-6361/201731107](https://doi.org/10.1051/0004-6361/201731107)
- . 2019, *A&A*, 625, A150, doi: [10.1051/0004-6361/201834539](https://doi.org/10.1051/0004-6361/201834539)
- Wang, M.-T., & Liu, H.-G. 2024, *AJ*, 168, 31, doi: [10.3847/1538-3881/ad4a60](https://doi.org/10.3847/1538-3881/ad4a60)
- Wes McKinney. 2010, in *Proceedings of the 9th Python in Science Conference*, ed. Stéfan van der Walt & Jarrod Millman, 56 – 61, doi: [10.25080/Majora-92bf1922-00a](https://doi.org/10.25080/Majora-92bf1922-00a)
- Windemuth, D., Agol, E., Carter, J., et al. 2019, *MNRAS*, 490, 1313, doi: [10.1093/mnras/stz2637](https://doi.org/10.1093/mnras/stz2637)
- Zorotovic, M., & Schreiber, M. R. 2013, *A&A*, 549, A95, doi: [10.1051/0004-6361/201220321](https://doi.org/10.1051/0004-6361/201220321)